

Basal Ganglia-Spinal Cord Pathway that Commands Locomotor Gait Asymmetries

Jared M. Cregg^{1,*}, Simrandeep K. Sidhu¹, Roberto Leiras¹, and Ole Kiehn^{1,2,*}

¹Department of Neuroscience, University of Copenhagen, 2200 Copenhagen, Denmark

²Department of Neuroscience, Karolinska Institutet, 17177 Stockholm, Sweden

*Co-corresponding authors

The basal ganglia are essential for executing motor actions. How the basal ganglia engage spinal motor networks has remained elusive. Medullary *Chx10* gigantocellular (Gi) neurons are required for turning gait programs, suggesting that turning gaits organized by the basal ganglia are executed via this descending pathway. Performing deep brainstem recordings of *Chx10* Gi Ca^{2+} activity in mice, we show that striatal projection neurons initiate turning gaits via a dominant crossed pathway to *Chx10* Gi neurons on the contralateral side. Intersectoral viral tracing and cell type-specific modulation uncovered the principal basal ganglia-spinal cord pathway for locomotor asymmetries in mammals: basal ganglia → pontine nucleus oralis (PnO) → *Chx10* Gi → spinal cord. Modulating the restricted PnO → *Chx10* Gi pathway restored turning competence in mice with striatal dopamine depletion, implicating this pathway as the motor substrate for debilitating turning deficits in Parkinson's disease. Our results reveal the stratified circuit architecture underlying a critical motor program.

INTRODUCTION

The basal ganglia are essential for motor action commitment. Basal ganglia control of motor actions has traditionally been examined in the context of cortico-striatal-thalamocortical loops. Nonetheless, the brainstem represents a major target of basal ganglia output (1, 2). Within the brainstem, diverse motor programs organize specific actions, including visual saccades, head direction, reach/grasp, orofacial movements, and locomotion (3–7). Previous work has utilized unitary recordings, electrical stimulation, optogenetic manipulations, and/or pharmacology (8–13) to indicate that basal ganglia control over motor programs operates via nigral disinhibition of target structures (14–18). Nevertheless, it remains crucial to delineate how the basal ganglia interface with specific brainstem motor pathways, and to identify the distinct circuit motifs that facilitate execution of motor actions at the spinal level (7, 19).

The basal ganglia are especially critical for locomotion (3, 5, 7). Locomotion requires precise rhythm and coordination which arises largely due to network properties intrinsic to the spinal cord itself (5, 20, 21). Recent data has revealed that distinct aspects of locomotor control are recruited via specific populations of brainstem reticulospinal neurons, including those responsible for locomotor initiation, speed, stop, and turn (5, 22–28). In particular, these data show that excitatory *Chx10* Gi reticulospinal projection neurons in

the medulla are required for turning gait asymmetries (25). The primacy of locomotion is exemplified in Parkinsonian patients, which exhibit a number of locomotor abnormalities including bradykinesia, freezing of gait, and exacerbated turning deficits (29–33). Turning gait deficits are especially prominent in advanced stages of Parkinson's disease (PD), representing a defining feature of PD gait (34). Turning in PD is characterized by increased turning duration, an increased number of small steps to complete a turn, and impaired rotational coordination (29, 33, 35, 36).

Using Ca^{2+} recording, intersectoral viral tracing, and gain- and loss-of-function optogenetic experiments in freely moving mice, we reveal that a PnO → *Chx10* Gi → spinal cord pathway is largely responsible for basal ganglia-induced turns. Furthermore, we used this specific pathway information to demonstrate the possibility of restoring turning competence in an experimental Parkinsonian mouse model. These data provide a direct circuit level explanation for basal ganglia induced turns, and turning deficits observed in basal ganglia disorders.

RESULTS

Brainstem *Chx10* Gi neurons encode turning gait asymmetries.

Medullary *Chx10*-lineage gigantocellular (*Chx10* Gi) neurons represent a reticulospinal command line required for turning (25). Unilateral activation of *Chx10* Gi neurons causes turning toward the ipsilateral side, whereas unilateral inhibition causes turning toward the contralateral side (25, 28). *Chx10* Gi neurons are located dorsomedial to LPGi (37), where a separate population of reticulospinal neurons has been implicated in locomotor initiation and speed (24, 38). How *Chx10* Gi neurons encode turning remains unresolved—are spontaneous turns accomplished by increasing *Chx10* Gi activity on the side of the turn, or decreasing *Chx10* Gi activity on the contralateral side? To investigate this, we performed deep brainstem GCaMP Ca^{2+} recording of *Chx10* Gi neurons in freely moving mice using endoscopic imaging and fiber photometry (Figure 1A).

Endoscopic Ca^{2+} imaging revealed that single *Chx10* Gi neurons encode turning velocity (Figures 1A–D, Supplementary Video 1). Of 7 cells obtained from 5 mice, 5 cells exhibited a significant cross-correlation between body angular ve-

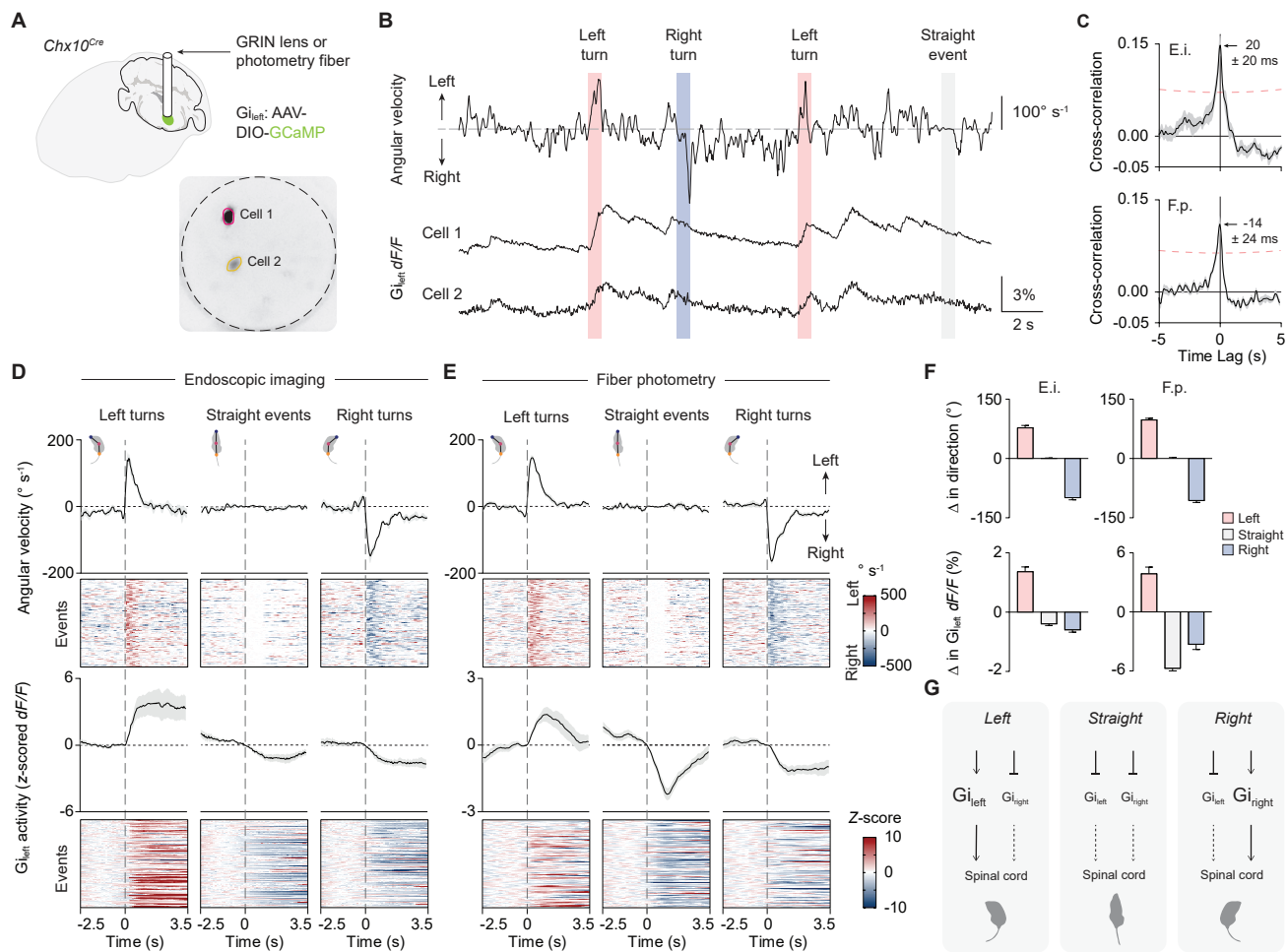


Figure 1. Brainstem *Chx10* Gi neurons encode turning gait asymmetries. **A**, Schematic of *Chx10* Gi_{left} GCaMP recording. Example endoscopic Ca²⁺ imaging field of view (inverted maximum dF/F projection). **B**, Example dF/F traces from cells in (A) with concurrent tracking of body angular velocity. *Chx10* Gi_{left} neuronal Ca²⁺ activity correlated with left turns, and was anti-correlated with right turns. **C**, Top, Cross-correlation between body angular velocity and *Chx10* Gi_{left} ddF/F activity obtained from endoscopic imaging (E.i.; n = 5 neurons from 4 mice). Bottom, Cross-correlation between body angular velocity and *Chx10* Gi_{left} ddF/F activity obtained using fiber photometry (F.p.; n = 14 mice). A negative time lag indicates that the ddF/F signal leads the angular velocity signal. Dashed red lines represent bounds for significant correlation. **D–E**, Spontaneous left turns, straight events, and right turns were segmented from angular velocity time series. Left turns were associated with an increase in *Chx10* Gi_{left} activity, whereas straight events and right turns were associated with a decrease in *Chx10* Gi_{left} activity. Endoscopic imaging: n = 5 neurons from 4 mice, 20 left turns, 20 straight events, and 20 right turns for each mouse. Fiber photometry: n = 14 mice, 10 left turns, 10 straight events, and 10 right turns for each mouse. Red denotes an increase in angular velocity (left turn) or an increase in z-score. Blue signifies a decrease in angular velocity (right turn) or decrease in z-score. **F**, Top, Change in direction associated with spontaneous left turns, straight events, or right turns segmented from angular velocity time series. Bottom, Change in *Chx10* Gi_{left} dF/F activity associated with spontaneous left turns, straight events, or right turns. Endoscopic imaging: n = 5 neurons from 4 mice. Fiber photometry: n = 14 mice. See Supplementary Table 1 for full statistical analysis. **G**, Model for *Chx10* Gi activity during spontaneous changes in locomotor direction. Spontaneous left turns are associated with both an increase in *Chx10* Gi_{left} activity as well as a decrease in *Chx10* Gi_{right} activity.

larity and ddF/F (Figure 1C). Rise in Ca²⁺ activity preceded turn onset, where cross-correlation surpassed the threshold for statistical significance (red dashed line in Figure 1C) at -400 ± 115 ms and exhibited a peak correlation at 20 ± 20 ms (Figure 1C). We segmented spontaneous left turns, straight events, and right turns from angular velocity profiles (Figure 1D, Supplementary Video 2). Spontaneous left turns (peak angular velocity greater than 200° s^{-1}) were correlated with an increase in dF/F activity of cells recorded in Gi_{left}, whereas right turns (less than $-200^\circ \text{ s}^{-1}$) were associated with a decrease in Gi_{left} dF/F activity (Figures 1D,F, Supple-

mentary Table 1). Moreover, straight events ($\pm 20^\circ \text{ s}^{-1}$) were also correlated with a decrease in Gi_{left} dF/F activity.

Fiber photometry revealed a direct correspondence between activity of single *Chx10* Gi neurons and activity at the population level. *Chx10* Gi_{left} population Ca²⁺ activity correlated with spontaneous leftward movements and was anti-correlated with rightward movements (Figures 1C,E). In 14 of 14 mice, the rise in Ca²⁺ activity preceded turn onset, with a significant cross-correlation between body angular velocity and ddF/F at -240 ± 53 ms and a peak correlation

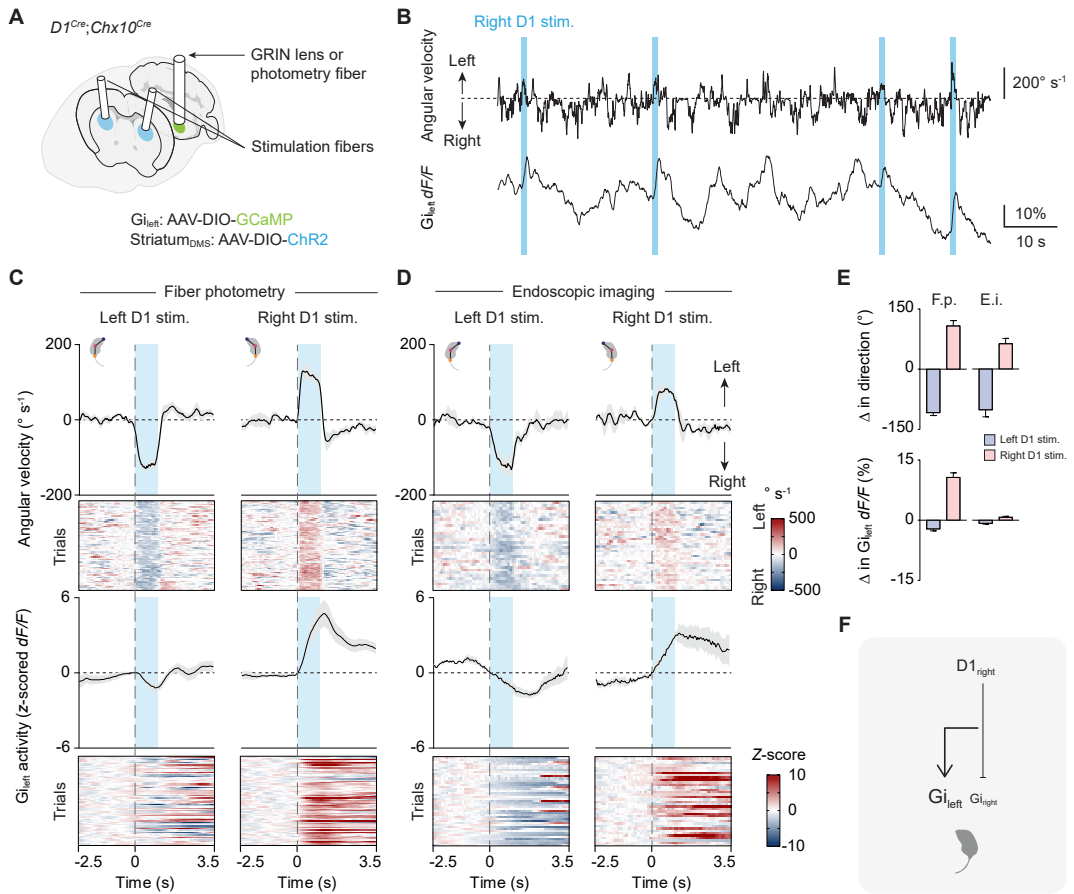


Figure 2. Stereotypic modulation of *Chx10* Gi activity via unilateral activation of D1 SPNs. **A**, Schematic of *Chx10* $G_{i\text{left}}$ GCaMP recording with optogenetic stimulation of left or right D1 SPNs. **B**, Example fiber photometry trace with concurrent tracking of body angular velocity. *Chx10* $G_{i\text{left}}$ activity correlated with left turns, and was anti-correlated with right turns. Stimulation of right D1 SPNs evoked left turns accompanied by an increase in *Chx10* $G_{i\text{left}}$ activity. **C-D**, Stimulation of D1 SPNs evoked contraversive turns, with an increase in *Chx10* Gi activity contralateral to the stimulation and decrease in *Chx10* Gi activity ipsilateral to the stimulation. Fiber photometry: $n = 7$ mice; 10 left and right D1 stimulation trials for each mouse. Endoscopic imaging: Left D1 stim; $n = 3$ cells from 2 mice; 12-20 trials for each mouse. Right D1 stim; $n = 3$ cells from 3 mice; 7-20 trials for each mouse. **E**, Top, Change in direction associated with 1 s ChR2 stimulation of left or right D1 SPNs. Bottom, Change in *Chx10* $G_{i\text{left}}$ dF/F activity associated with 1 s ChR2 stimulation of left or right D1 SPNs. The magnitude of the change in dF/F was greater for D1_{right} versus D1_{left} stimulation trials * $P = 0.037$; two-tailed paired t-test; $n = 7$ mice. See Supplementary Table 1 for full statistical analysis. **F**, Model for locomotor asymmetries caused by stimulation of D1 SPNs. Optogenetic stimulation of D1 SPNs has a dominant contralateral excitatory effect on *Chx10* Gi neurons, as well as a weaker ipsilateral inhibitory effect.

at -14 ± 24 ms (Figure 1C). Furthermore, spontaneous left turns segmented from angular velocity profiles were correlated with an increase in *Chx10* $G_{i\text{left}}$ population Ca^{2+} activity, whereas right turns were associated with a decrease in Ca^{2+} population activity (Figures 1E,F, Supplementary Video 2, Supplementary Table 1). Similar to single cell recordings, straight events were also correlated with a decrease in Ca^{2+} population activity (Figures 1E,F). These data indicate that *Chx10* Gi population activity encodes body angular velocity. Spontaneous turns are associated with bilateral modulation of *Chx10* Gi activity: an increase in activity on the side of the turn and a decrease in activity on the contralateral side (Figures 1F,G), consistent with unilateral *Chx10* Gi gain- and loss-of-function experiments (25, 28).

Chx10 Gi neurons encode striatal turning gait asymmetries.

Hemispheric imbalances in the activity of dopamine receptor 1 (D1) or dopamine receptor 2 (D2) striatal projection neurons (SPNs) induce locomotor gait asymmetries (1, 39, 40). We established a paradigm for studying whether such gait asymmetries generated by the striatum are encoded by *Chx10* Gi activity: GCaMP Ca^{2+} recording was used to assay *Chx10* $G_{i\text{left}}$ neuronal activity in response to optogenetic (channelrhodopsin-2, ChR2) stimulation of D1 or D2 SPNs on the left or right side (Figure 2A, Supplementary Figures 1, 2). Here, we obtained selective expression of ChR2 in either D1 or D2 SPNs while recording *Chx10* Gi calcium activity by leveraging the observation that $D1^{\text{Cre}}$ and $D2^{\text{Cre}}$, and $Chx10^{\text{Cre}}$ alleles exhibit non-overlapping Cre expression within the striatum and Gi, respectively (Supplementary Figures 1A-C). This enabled distinct targeting of these populations with viral vectors in $D1^{\text{Cre}};Chx10^{\text{Cre}}$ or $D2^{\text{Cre}};Chx10^{\text{Cre}}$ dual-allelic mice (Supplementary Figures 1D,E).

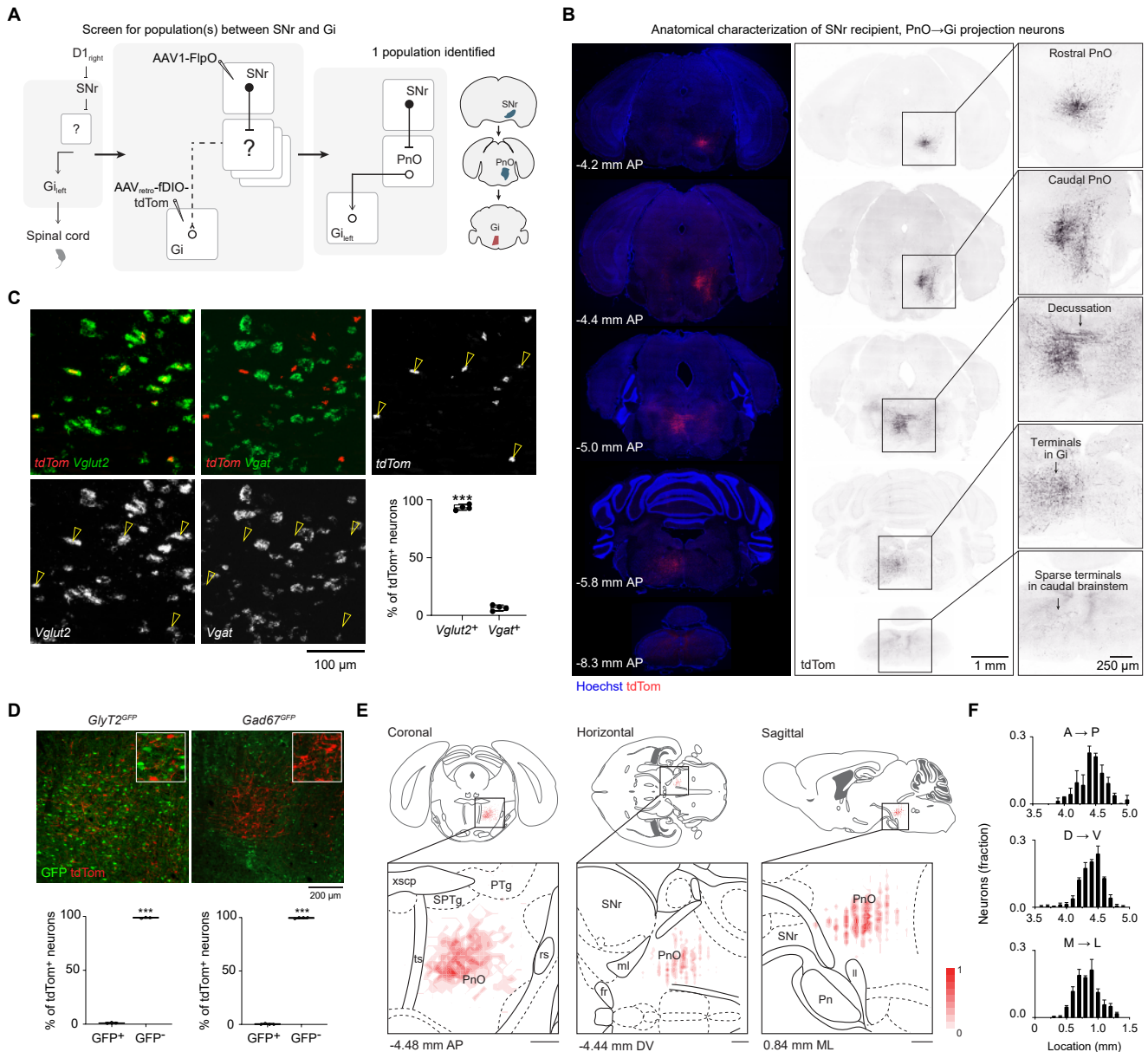


Figure 3. Commissural Vglut2⁺ neurons in PnO link SNr to Gi. **A**, Viral screening strategy for identifying link between SNr and Gi. AAV_{retro-fDIO-tdTom} was injected in Gi_{left}, followed by injection of AAV1-FlpO in SNr_{right}. This screen uncovered only one neuronal population which links SNr to Gi located in the pontine nucleus oralis (PnO_{right}, ipsilateral to SNr and contralateral to Gi). **B**, Anatomy of SNr recipient, PnO → Gi projection neurons. Neurons exhibit caudally projecting axons which decussate at -5.0 mm AP and terminate in the contralateral Gi. Caudal brainstem sections exhibit only sparse axonal projections. **C**, Triple *in situ* hybridization for tdTom, Vglut2, and Vgat indicates 93.4 ± 1.2% of tdTom⁺ (SNr recipient, PnO → Gi projection) neurons co-expressed Vglut2 whereas 6.6 ± 1.2% of tdTom⁺ neurons co-expressed Vgat. ***P = 4.2 × 10⁻⁵; two-tailed paired t-test; n = 4 mice. See also, Supplementary Table 1. **D**, tdTom labeling of SNr recipient, PnO → Gi projection neurons in GlyT2^{GFP} (left) or Gad67^{GFP} (right) mice. SNr recipient, PnO → Gi projection (tdTom⁺) neurons are predominantly GFP⁺, indicating they are not glycinergic or GABAergic. GlyT2^{GFP}, ***P = 3.0 × 10⁻⁵; Gad67^{GFP}, ***P = 4.0 × 10⁻⁷; two-tailed paired t-test; n = 3 mice for GlyT2^{GFP} and n = 4 mice for Gad67^{GFP}. **E**, Density plots representing the location of soma in the coronal, horizontal, and sagittal planes. Population data are superimposed on plates redrawn from Paxinos and Franklin's reference atlas (37). Plates were selected based on the mean AP, DV, or ML value of all PnO-Vglut2_{contra} neurons registered. **F**, Quantification of PnO-Vglut2_{contra} neurons in the AP, DV, and ML axis relative to bregma, n = 3 mice.

In accordance with previous experiments (1, 39), stimulation of right D1 SPNs in the dorsomedial striatum caused left turns (contraversive turns, Figures 2B-E, Supplementary Video 3). These left turns were accompanied by a marked increase in *Chx10* Gi_{left} dF/F activity at the population level and at the level of single neurons (Figures 2B-E, Supplementary Video 3). Stimulation of left D1 SPNs initiated right turns associated with a decrease in *Chx10* Gi_{left} dF/F activity (Figures 2B-E, Supplementary Video 3). Conversely, stimulation of left D2 SPNs caused left (ipsiversive) turns accompanied by an increase in *Chx10* Gi_{left} population Ca²⁺ activity, whereas stimulation of right D2 SPNs caused right turns associated with a decrease in *Chx10* Gi_{left} dF/F activity (Supplementary Figures 2A-C, Supplementary Video 3). These data show that unilateral stimulation of D1 or D2 SPNs modulates *Chx10* Gi activity bilaterally; stimulation of D1 SPNs caused both an increase in dF/F activity of *Chx10* Gi neurons on the contralateral side as well as a decrease in *Chx10* Gi activity on the ipsilateral side. The magnitude of the change in dF/F activity was greater for contralateral D1 stimulation trials (Figures 2C-E), suggesting that a crossed pathway is dominant in driving the motor action. Together these data demonstrate that *Chx10* Gi neurons execute basal ganglia-evoked turns, offering parsimonious models as to how this is coordinated by descending *Chx10* reticulospinal projections (Figure 2F, Supplementary Figure 2D).

A defined population of commissural pontine projection neurons links basal ganglia output to *Chx10* Gi.

The observation that *Chx10* Gi neurons exhibit stereotyped responses to unilateral activation of D1 or D2 SPNs (Figure 2, Supplementary Figure 2) suggests a discrete pathway linking basal ganglia output, i.e. the substantia nigra pars reticulata (SNr), to *Chx10* Gi. However, our previous monosynaptic rabies tracing showed that *Chx10* Gi neurons do not receive direct input from SNr or any other basal ganglia neurons (25), indicating that the basal ganglia acts on *Chx10* Gi neurons via an intermediate pathway link (Figure 3A).

To identify candidate neuronal population(s) that link the basal ganglia with *Chx10* Gi neurons we used an intersectional viral screening strategy (Figure 3A). We targeted SNr as the dominant output nucleus of the basal ganglia (2). A retrograde virus, AAV_{retro}-fDIO-tdTom, was injected in Gi_{left} followed by an anterograde transsynaptic tracer (1, 41, 42), AAV1-FlpO, injected in SNr_{right} (Figure 3A). Here, AAV1 transduces downstream targets of SNr with FlpO, and if these target neurons also project to Gi, they will be labeled with tdTom. This screen uncovered only one cluster of neurons within the anatomical boundaries of the pontine nucleus oralis (37) (PnO_{right}, ipsilateral to SNr and contralateral to Gi), which is also known as the rostral pontine reticular nucleus (PRNr) (Figures 3A,B) (43). SNr recipient, PnO → Gi projection neurons are commissural, exhibiting descending axons that cross the midline caudally at the level of the PnC, which then descend further and arborize in the contralateral Gi (Figure 3B). Identification of neurons in PnO is consistent

with our previous work, which identified PnO as one of 40 nuclei with monosynaptic input to *Chx10* Gi (25).

PnO is composed of multiple excitatory and inhibitory projection subtypes (Figures 3C,D). Using triple *in situ* hybridization for *tdTom*, vesicular glutamate transporter (*Vglut2*), and vesicular inhibitory amino acid transporter (*Vgat*), we found that 93.4 ± 1.2% of SNr recipient, PnO → Gi projection neurons were *Vglut2* positive and *Vgat* negative (Figure 3C), indicating a predominantly glutamatergic identity. Indeed, a vast majority of SNr recipient, PnO → Gi projection neurons lacked GFP expression in *GlyT2*^{GFP} or *Gad67*^{GFP} mice (Figure 3D). We henceforth refer to this subpopulation of PnO projection neurons as PnO-Vglut2_{contra}. Together these data show that inhibitory basal ganglia output neurons in SNr connect to excitatory *Chx10* Gi neurons (22, 25) via a crossed excitatory glutamatergic hub located in the brainstem PnO.

To assess the possibility at a behavioral level that PnO-Vglut2_{contra} neurons are involved in turning, we performed gain- and loss-of-function optogenetic studies using ChR2 or GtACR2 (Figure 4A). ChR2 stimulation (40 Hz) of PnO-Vglut2_{contra} neurons produced robust turning toward the contralateral side (Figures 4B-D, Supplementary Video 4), corresponding to crossed excitatory action on *Chx10* Gi_{contra} neurons. Notably, in contrast to stimulation of D1 or D2 SPNs (Supplementary Figure 3, Supplementary Video 3), ChR2-mediated stimulation of PnO-Vglut2_{contra} neurons evoked contralateral turning of the body with limited effect on axial (head or trunk) posture (Figures 4B-D, Supplementary Figure 4). Varying the stimulation frequency allowed tight control of turning kinematics, with lower stimulation frequencies (5-20 Hz) inducing smaller changes in angular velocity accompanied by larger turning radii (Figures 4E-H, Supplementary Video 5). To confirm that this phenotype was linked to a glutamatergic identity, we used an INTRSECT strategy (44) to express ChR2 in PnO-Vglut2_{contra} neurons based both on input (SNr_{ipsi})/output (Gi_{contra}) connectivity as well as Vglut2 identity (Supplementary Figure 4A). Stimulation of PnO-Vglut2_{contra} neurons using this approach recapitulated the contralateral turning phenotype (Supplementary Figure 4B). Furthermore, using an INTRSECT strategy, we confirmed that *Chx10* Gi neurons act as the postsynaptic target of PnO-Vglut2_{contra} neurons (Supplementary Figures 4C,D). Finally, GtACR2 photoinhibition of PnO-Vglut2_{contra} neurons caused robust turning toward the ipsilateral side (Figures 4I-K, Supplementary Video 4). This latter finding indicates that PnO-Vglut2_{contra} neurons are tonically active at rest, such that inhibitory tone from SNr would modulate the activity of PnO-Vglut2_{contra} neurons bidirectionally: decreased SNr activity would increase the activity of PnO-Vglut2_{contra} neurons, whereas increased SNr activity would decrease the activity of PnO-Vglut2_{contra} neurons.

To evaluate the necessity of the PnO → Gi pathway for turning, we chronically silenced PnO-Vglut2_{contra} neurons using viral-mediated expression of tetanus-toxin light chain (TeLC; Figure 4L). TeLC expression caused strong ipsilat-

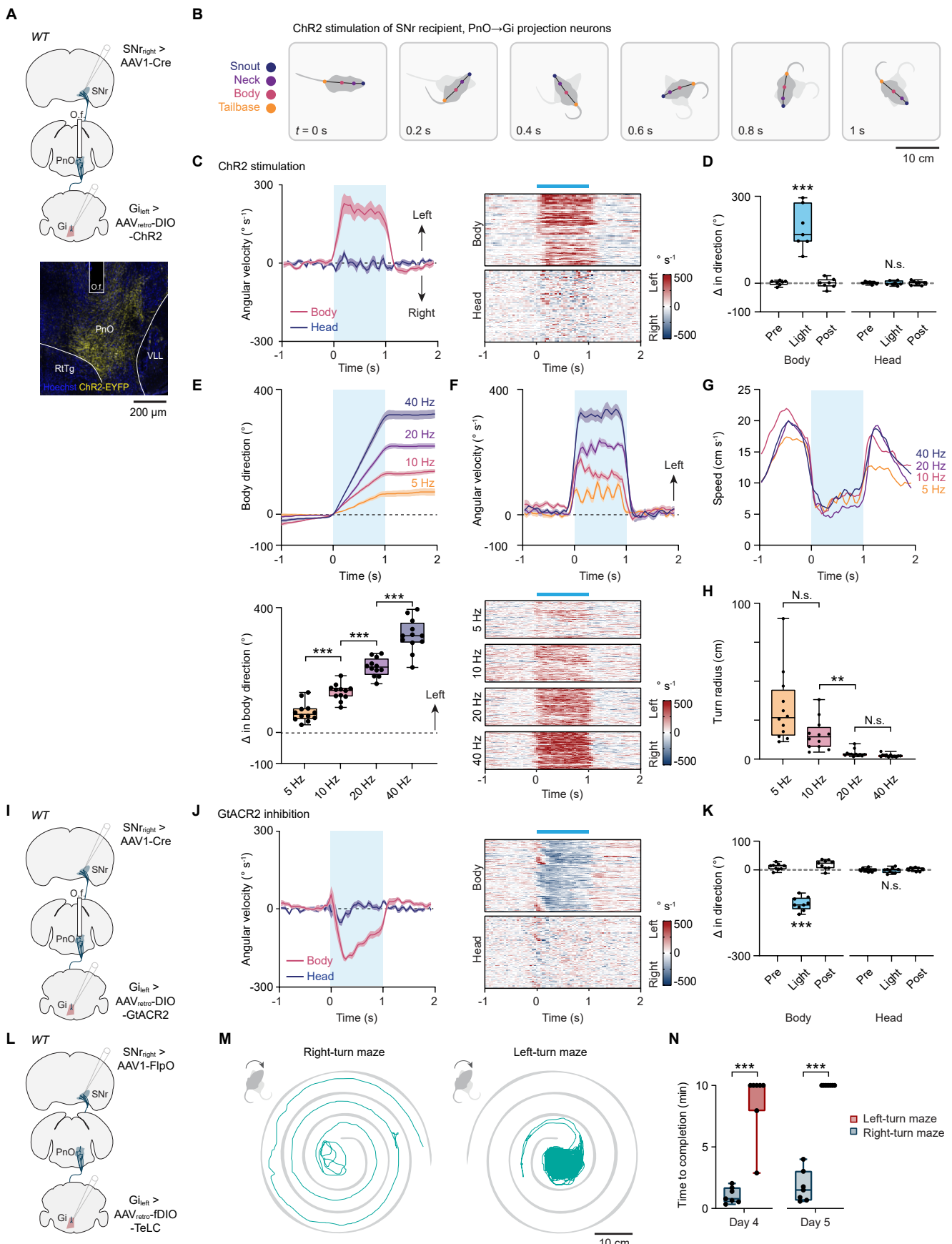


Figure 4. (Caption on the next page)

Figure 4. Selective manipulation of PnO-Vglut2_{contra} neurons modulates turning bidirectionally. **A**, Strategy for ChR2 stimulation of PnO-Vglut2_{contra} neurons. Example of ChR2-EYFP expression and optic fiber (O.f.) implantation in the right PnO. Image is representative of $n = 19$ mice. **B**, ChR2 stimulation of PnO-Vglut2_{contra} neurons caused contralateral rotation of the body but had little effect on head or trunk (axial) posture. **C-D**, Quantification of ChR2 stimulation. Body, $***P = 8.9 \times 10^{-4}$; head, $P = 0.96$; one-way ANOVA with Tukey's multiple comparison test; $n = 7$ mice (where n is the average of 10 trials for each mouse). **E**, Change in body direction associated with 1 s ChR2 stimulation at different frequencies. 5 Hz vs. 10 Hz, $***P = 6.1 \times 10^{-5}$; 10 Hz vs. 20 Hz, $***P = 7.6 \times 10^{-6}$; 20 Hz vs. 40 Hz, $***P = 3.1 \times 10^{-5}$; one-way repeated measures ANOVA with Tukey's multiple comparison test; $n = 12$ mice (where n is the average of 10 trials for each mouse). **F**, Top, Average body angular velocity associated with 1 s ChR2 stimulation at different frequencies. Bottom, Trial-by-trial analysis of angular velocity at different frequencies. **G**, ChR2 stimulation was accompanied by a reduction in locomotor speed independent of the frequency of stimulation, see (25). Speed profiles represent the average of $n = 12$ mice with 10 trials for each mouse. **H**, Average turning radius during 1 s ChR2 stimulation at different frequencies. 5 Hz vs. 10 Hz, no significance; 10 Hz vs. 20 Hz, $**P = 0.0089$; 20 Hz vs. 40 Hz, no significance; one-way repeated measures ANOVA with Tukey's multiple comparison test; $n = 12$ mice (where n is the average of 10 trials for each mouse). **I**, Strategy for GtACR2 inhibition of PnO-Vglut2_{contra} neurons. **J-K**, GtACR2 inhibition of PnO-Vglut2_{contra} neurons caused ipsilateral rotation of the body. Body, $***P = 4.4 \times 10^{-7}$; head, $P = 0.94$; one-way ANOVA with Tukey's multiple comparison test; $n = 9$ mice (where n is the average of 10 trials for each mouse). **L-N**, Inhibition of PnO-Vglut2_{contra} neurons with TeLC caused ipsilateral turning, and impaired exploration of a contralateral (left-turn) maze. Day 4, $***P = 6.0 \times 10^{-4}$; Day 5, $***P = 2.8 \times 10^{-6}$; two-tailed paired t-test; $n = 7$ mice.

eral (right) turning within four days of viral delivery (Figures 4L-N). Mice were then tested in spiral-shaped mazes (Figure 4M), which the mice were allowed to explore to completion or until 10 min had elapsed. Unaffected mice rapidly completed both left- and right-turn mazes (25). In contrast, mice with chronic silencing of PnO-Vglut2_{contra} neurons readily completed the right-turn (ipsilateral) maze but could not complete the left-turn (contralateral) maze (Figures 4L-N). These experiments show that mice cannot compensate for a loss of PnO-Vglut2_{contra} function; PnO-Vglut2_{contra} neurons are requisite for natural exploratory behavior.

Basal ganglia mediated turning gaits act predominantly via PnO.

We undertook a series of optogenetic studies to further understand the SNr → PnO projection. Previous work has demonstrated that broad inhibition of SNr neurons induces contralateral turning (45, 46). To confirm and benchmark this phenotype, we broadly transduced SNr with AAV-DIO-GtACR2 (*Vgat*^{Cre} > DIO-GtACR2, Figures 5A,B). Broad GtACR2 inhibition of SNr neurons produced robust contralateral rotation which consisted of changes in body orientation mediated by the limbs as well as contraction of the axial head and trunk musculature (Figures 5C,D). Compared with broad SNr transduction, retrograde transduction of SNr by injection of AAV_{retro}-DIO-GtACR2 in PnO labeled only a subpopulation of SNr neurons localized within a caudo-medial domain (Figure 5B). GtACR2 inhibition of this restricted SNr → PnO population evoked contralateral turning, accounting for approximately 70% ($68.0 \pm 7.0\%$, $n = 7$ mice) of the limb-based turning phenotype obtained by broad SNr inhibition (Figure 5D). Notably, whereas broad SNr inhibition caused limb-based changes in body orientation as well as contraction of the head and trunk musculature, inhibition of the restricted SNr → PnO population evoked only a limb-based contralateral rotation of the body without a prominent effect on axial (head or trunk) posture (Figures 5C,D, Supplementary Video 6).

Broad activation of SNr likely also recruits axial motor networks via projections to the superior colliculus (47, 48). To investigate this possibility, we retrogradely transduced SNr by injection of AAV_{retro}-DIO-GtACR2 in SC, labeling a subpopulation of SNr neurons localized within a rostral-lateral domain (Figure 5B). GtACR2 inhibition of this restricted SNr → SC population evoked contralateral turning, and recapitulated changes in head and trunk posture that were associated with broad SNr inhibition (Figures 5C,D). Notably, the limb-based turning phenotype associated with inhibition of SNr → SC neurons accounted for only $35.8 \pm 5.6\%$ ($n = 7$ mice) of that associated with broad SNr inhibition, and was substantially reduced compared with specific SNr → PnO inhibition (Figure 5D). These data indicate that limb-based changes in body orientation can be largely dissociated from turning of the head at the level of brainstem motor circuits; the SNr → PnO pathway controls limb-based body orientation, whereas the SNr → SC pathway primarily controls head orientation. The outputs of these two pathways cross the midline and re-converge at the level of reticulospinal populations in the contralateral Gi, where *Chx10* subpopulation(s) control limb-based body orientation and/or head orientation, respectively (Supplementary Figures 4C,D) (25, 28).

Mirroring the effect of GtACR2 inhibition, broad optogenetic activation of inhibitory SNr neurons produced ipsilateral turning (Supplementary Figure 5A). ChR2 stimulation of inhibitory SNr neurons retrogradely transduced from PnO accounted for approximately 70% ($68.5 \pm 2.9\%$) of the ipsilateral turning phenotype obtained by directly targeting SNr (Supplementary Figure 5B). Notably, this effect was likely mediated through SNr → PnO projections and not via potential collaterals since stimulation of inhibitory SNr terminals in PnO also evoked ipsilateral turning (Supplementary Figure 5C), accounting for $66.0 \pm 4.7\%$ of the phenotype associated with broad SNr stimulation.

Together, these data show that basal ganglia-evoked turning gait asymmetries act predominantly through neurons located in PnO. Moreover, the data show that the SNr → PnO basal ganglia output channel is specific for limb-based turn-

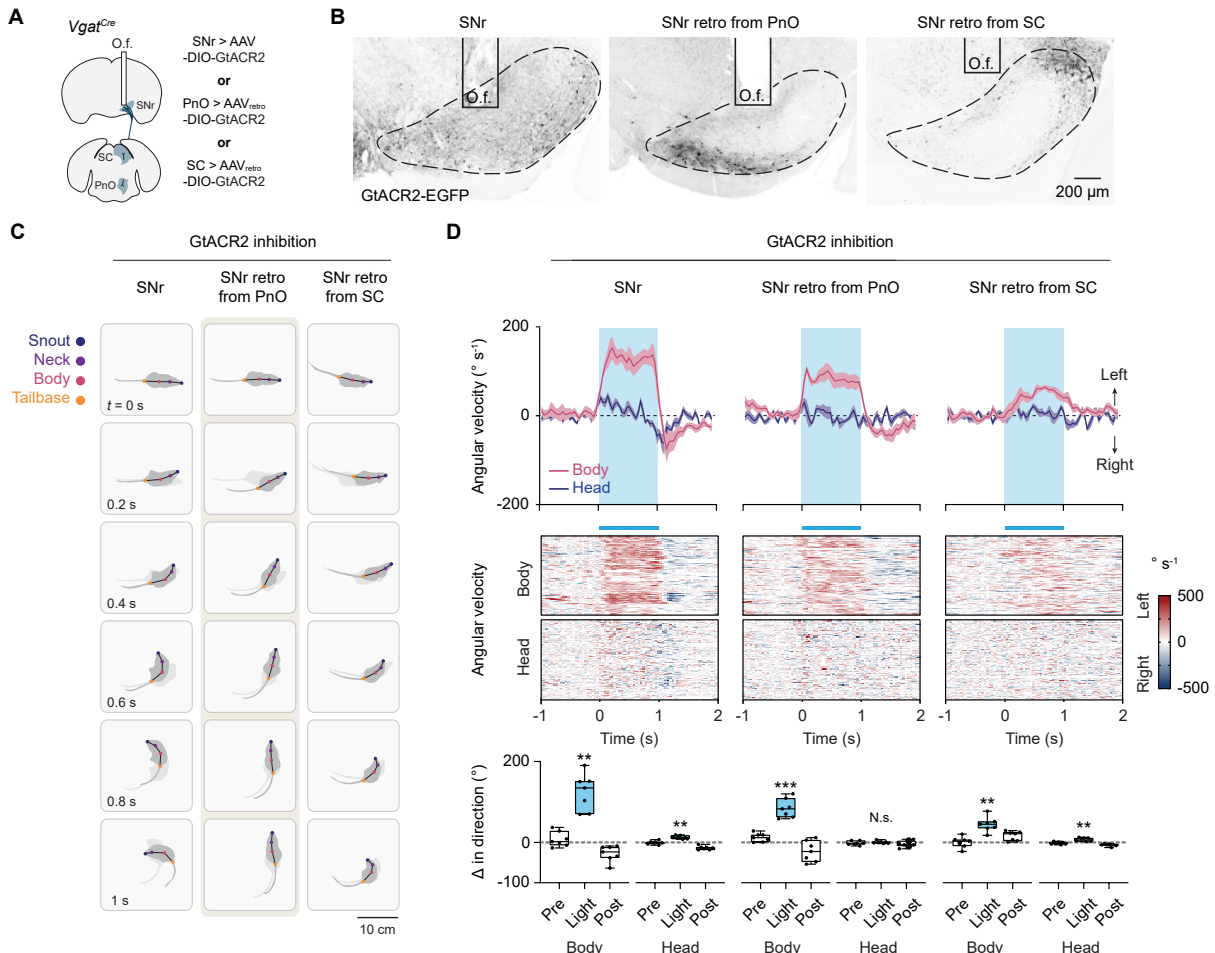


Figure 5. Basal ganglia turning gait asymmetries act predominantly via PnO. **A**, Strategies for GtACR2 transduction of a bulk Vgat⁺ SNr population, or specific populations of Vgat⁺ SNr → PnO or SNr → SC projection neurons. **B**, Examples of GtACR2 transduction and fiber placement using strategies in **(A)**. Vgat⁺ neurons labeled via retrograde transduction from PnO exhibited localization within a caudomedial domain, whereas Vgat⁺ neurons labeled via retrograde transduction from SC exhibited localization within a rostralateral domain. **C**, Optogenetic inhibition of SNr caused limb-based changes in body orientation as well as contraction of the trunk musculature. Selective optogenetic inhibition of SNr → PnO projection neurons evoked a strong limb-based contralateral rotation of the body without a prominent effect on axial (head or trunk) posture. Selective optogenetic inhibition of SNr → SC projection neurons caused weak limb-based changes in body orientation, as well as contraction of the head and trunk musculature. **D**, *Left*, Inhibition of a bulk Vgat⁺ SNr population. Body, **P = 0.0013; head, **P = 0.002; one-way ANOVA with Tukey's multiple comparison test. *Center*, selective inhibition of SNr → PnO projection neurons. Body, ***P = 1.8 x 10⁻⁴; head, P = 0.70; one-way ANOVA with Tukey's multiple comparison test; n = 7 mice (where n is the average of 10 trials for each mouse). *Right*, selective inhibition of SNr → SC projection neurons. Body, **P = 0.0013; head, **P = 0.0056; one-way ANOVA with Tukey's multiple comparison test. n = 7 mice for each experiment, where n is the average of 10 trials for each mouse.

ing mechanisms which act to promote hindlimb extensor tone, rather than those mechanisms that control axial bending, see Clegg et al. (25).

Reversing pathological asymmetries by targeting downstream motor nuclei.

Gait deficits are a defining characteristic of Parkinson's disease (31, 32). In advanced PD, turning deficits represent a hallmark symptom, characterized by increased turning duration, an increased number of small steps to complete a turn, and impaired rotational coordination (29, 33, 35, 36). Turning deficits are also observed in hemi-Parkinsonian mice after acute and chronic unilateral depletion of striatal dopamine, unilateral administration of the catecholaminergic neurotoxin

6-hydroxydopamine (6-OHDA) in the substantia nigra pars compacta, medial forebrain bundle, or striatum leads to increased turning toward the lesioned side and an exacerbated turning deficit toward the contralateral side (49–52). The brainstem motor substrate for turning deficits in PD is unknown; however, unilateral hypoactivity in the PnO → Chx10 Gi pathway could readily explain limb-based rotational phenotypes in hemi-Parkinsonism (53). We therefore set out to induce pathological asymmetries by unilateral 6-OHDA lesion of nigrostriatal projections, and reverse these asymmetries by modulation of the PnO → Chx10 Gi pathway.

We first addressed the role of Chx10 Gi neurons. To stimulate Chx10 Gi_{left} neurons, Chx10^{Cre} mice were injected

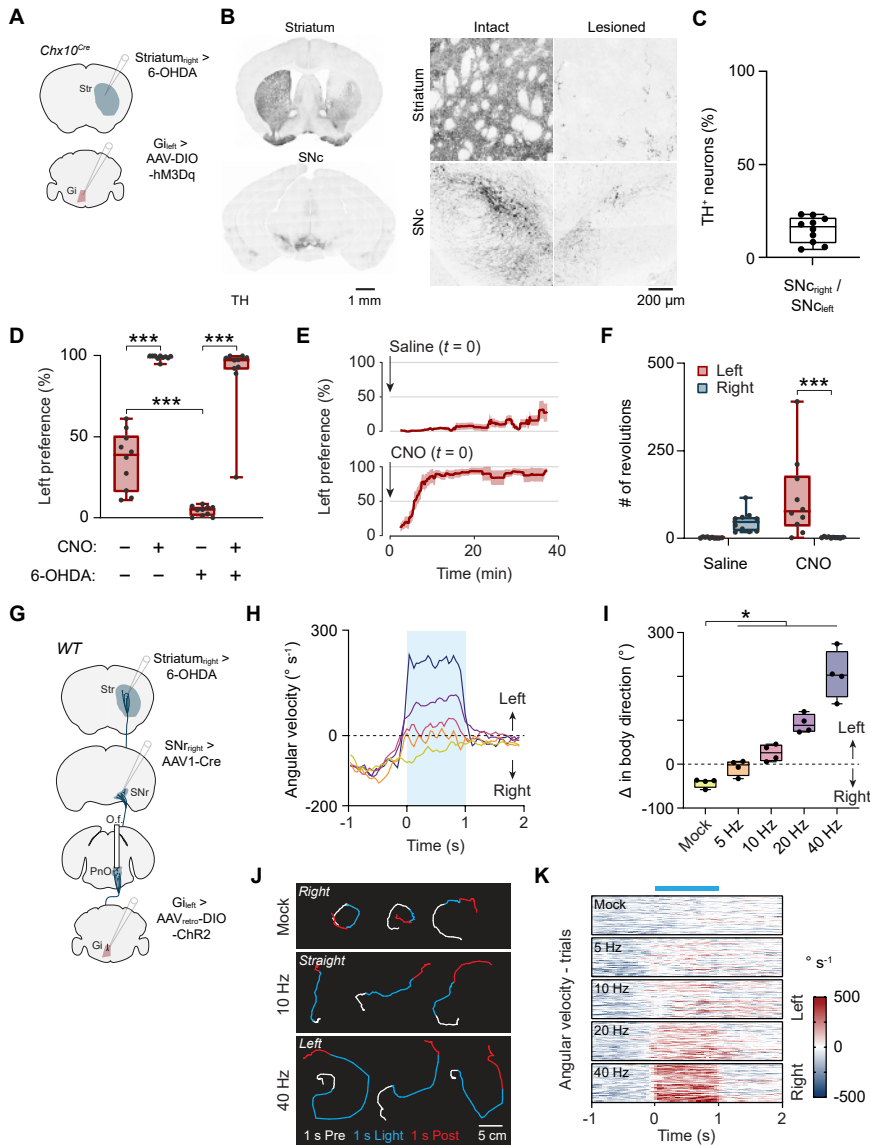


Figure 6. Restoration of contraversive turning gaits in mice with acute unilateral striatal dopamine depletion. **A**, Strategy for restoring contraversive turning in mice with unilateral striatal dopamine depletion. **B**, Unilateral 6-OHDA lesioned mice exhibited loss of dopaminergic (tyrosine hydroxylase positive, TH⁺) terminals in the ipsilateral striatum, and loss of TH⁺ neurons of the ipsilateral substantia nigra pars compacta (SNc). **C**, Quantification of 6-OHDA lesion efficacy. **D**, Analysis of left vs. right movement preference in the open field. –CNO/-6-OHDA vs. +CNO/-6-OHDA, *** P = 8.3×10^{-11} ; –CNO/-6-OHDA vs. –CNO/+6-OHDA, *** P = 1.7×10^{-4} ; –CNO/+6-OHDA vs. +CNO/+6-OHDA, *** P < 1.0×10^{-15} ; two-way ANOVA with Tukey's multiple comparison test; n = 10 mice. Pre-lesion data (–6-OHDA) is also presented in Supplementary Figure 6D. **E**, Mice with acute unilateral striatal dopamine depletion exhibited predominantly ipsiversive (right) movement preference. CNO administration at *t* = 0 reversed ipsiversive rotational biases in a time-dependent manner. **F**, Number of left and right revolutions quantified in mice with acute unilateral striatal dopamine depletion 10–40 min after injection of saline or CNO. CNO left vs. CNO right, *** P = 9.0×10^{-4} ; two-way ANOVA with Tukey's multiple comparison test; n = 10 mice. **G**, Strategy for testing the efficacy of PnO-Vglut2_{contra} neurons in restoring contraversive turning in mice with acute unilateral striatal dopamine depletion. **H**, Optogenetic stimulation of PnO-Vglut2_{contra} neurons reversed ipsilateral rotational biases, restoring straight locomotion at low frequencies (5 Hz, 10 Hz) and contralateral turning gaits at high frequencies (20 Hz, 40 Hz). **I**, Quantification of the change in body direction during 1 s mock stimulation or ChR2 stimulation at different frequencies. Mock vs. 5 Hz, * P = 0.021; Mock vs. 10 Hz, * P = 0.019; Mock vs. 20 Hz, * P = 0.012; Mock vs. 40 Hz, * P = 0.018; one-way repeated measures ANOVA with Tukey's multiple comparison test; n = 4 mice (where n is the average of 10 trials for each mouse). **J**, Example trajectories associated with mock stimulation (no light) or 1 s ChR2 stimulation. 10 Hz stimulation restored straight working during stimulation, while 40 Hz stimulation restored contralateral turning gaits. **K**, Trial-by-trial analysis of angular velocity during mock stimulation or ChR2 stimulation at different frequencies. Each plot contains 40 individual trials from n = 4 mice (10 trials per mouse).

unilaterally with excitatory DREADDS (DIO-hM3Dq) (Figure 6A, Supplementary Figure 6A). Under baseline (saline) conditions, mice showed close to symmetric turning. After activation of *Chx10* Gi_{left} neurons with CNO (1 mg kg⁻¹), mice exhibited turning towards the side of stimulation (the left side, see Cregg et al.) (25) (Supplementary Figures 6B,C). The same mice were then injected with 6-OHDA in the right dorsomedial striatum for acute (4-6 days after injection) or chronic (15-19 days after injection) models of hemi-Parkinsonism. Injection of 6-OHDA led to loss of dopaminergic (tyrosine hydroxylase positive, TH⁺) terminals in the striatum on the side of injection, and reduction of dopaminergic cell bodies in ipsilateral substantia nigra pars compacta (Figures 6B,C). Unilateral 6-OHDA lesioned mice exhibited a dominantly ipsiversive (right) turning preference in both the acute and chronic lesioned state (Figures 6D-F, Supplementary Figures 6D-F, Supplementary Video 7). Activation of *Chx10* Gi_{left} neurons with CNO (1 mg kg⁻¹) rapidly reversed the ipsiversive turning, restoring contraversive turning gaits (Figures 6D-F, Supplementary Figures 6D-F). The reversal developed slowly, with an early phase between 5-10 minutes after CNO administration where mice exhibited close to symmetric turning, which then developed into predominantly contraversive turning (Figure 6E, Supplementary Figure 6E, Supplementary Video 7). These experiments show that turning gait deficits induced by unilateral striatal dopamine depletion can be reversed by activation of *Chx10* Gi neurons.

We next investigated the contribution of PnO-Vglut2_{contra} neurons (Figure 6G, Supplementary Figure 6G). Graded ChR2 stimulation (5-40 Hz, pulse duration 15 ms, fixed amplitude) of PnO-Vglut2_{contra} neurons modulates the magnitude of turning in a frequency dependent manner (Figures 4E-H). A similar graded stimulation of PnO-Vglut2_{contra} neurons on the lesioned side in the acute or chronic phase of hemi-Parkinsonism reversed ipsiversive turning biases, restoring straight locomotion at low frequencies (5 Hz or 10 Hz in the acute and chronic phase) and contraversive turning gaits at high frequencies (20 Hz, 40 Hz) (Figures 6H-K, Supplementary Figures 6H-K, Supplementary Video 8). These data show that graded stimulation of PnO-Vglut2_{contra} neurons is sufficient to normalize gait asymmetries and to restore contralateral turning in hemi-Parkinsonian mice.

DISCUSSION

Our study reveals the functional organization of circuits that control left-right turning gait asymmetries. We show how the basal ganglia work in tandem with brainstem circuits to recruit spinal motor networks, providing a detailed account as to how the basal ganglia executes a complex movement. Recent insight that gait asymmetries are definitively controlled via a dedicated population of *Chx10* Gi neurons that projects directly to the spinal cord (25, 28) was key to establishing this motor pathway. Our results thus demonstrate how well-known basal ganglia-mediated turning gait asymmetries are produced, opening the possibility of addressing this question in the framework of brain-wide networks.

A classic model of basal ganglia control over motor actions holds that opponent pathways, the striatal direct and indirect pathways, enable bidirectional control over downstream motor programs (39, 55). In context of turning gait asymmetries, stimulation of direct pathway SPNs promotes contraversive turning and indirect pathway SPNs promotes ipsiversive turning (39). Furthermore, at the level of SNr, a dominant basal ganglia output, unilateral stimulation of inhibitory neurons promotes ipsiversive turning (54) and unilateral silencing promotes contraversive turning (46) (as we confirm here). The simplest model would posit that SNr bidirectionally modulates a specific population of downstream neurons around a setpoint of tonic activity. Indeed, we found that PnO-Vglut2_{contra} neurons can be modulated bidirectionally—through decreased or increased inhibitory input via a specific SNr → PnO channel—initiating either contraversive or ipsiversive turning, respectively. Therefore, decreased unilateral SNr activity caused by unilateral D1 activation would act to disinhibit PnO-Vglut2_{contra} neurons, allowing activation of contralateral *Chx10* Gi to initiate contraversive turns. In contrast, increased SNr activity by unilateral D2 activation would act to inhibit PnO-Vglut2_{contra} neurons leading to ipsiversive turns (Figure 7).

We observed bidirectional modulation of *Chx10* Gi population activity during spontaneous turns, with increased or decreased activity when the animals turn to the ipsilateral or contralateral side, respectively. Notably, we also observed a bilateral decrease in *Chx10* Gi activity during straight events. While we did not relate population activity to stop events (22), importantly, changes in population activity were not correlated with other types of active non-locomotor behaviors like grooming as previously described from single neuron recordings (56). The difficulties we encountered in performing reliable single neuron recording in Gi prevented us from addressing this issue further. However, most of the (few) cells we recorded using endoscopic imaging recapitulated the activity patterns observed in population recordings using fiber photometry. *Chx10* Gi neurons themselves enable bidirectional modulation of spinal locomotor network activity (22) (Figure 7). Together, these data imply that the mode of operation along the SNr → PnO-Vglut2_{contra} → *Chx10* Gi axis is resting tonic activity that can be decreased or increased to generate turns. Candidate mechanisms for resting tonic activity of PnO-Vglut2_{contra} or *Chx10* Gi neurons include those mechanisms demonstrated for SNr, where tonic activity depends on resting inward conductances (2, 57–60).

We identified excitatory PnO-Vglut2_{contra} neurons as a critical link interfacing between basal ganglia output and *Chx10* Gi reticulospinal neurons. Anatomical projection to the PnO from a restricted area of SNr has recently been described (2). However, the functional role of SNr-PnO projection neurons has not been determined. Various motor functions, including postural adjustment and motor immobility (61), have been suggested to be regulated by neurons in PnO. These and our data indicate that the greater PnO represents a heterogeneous pontine reticular nucleus composed of mul-

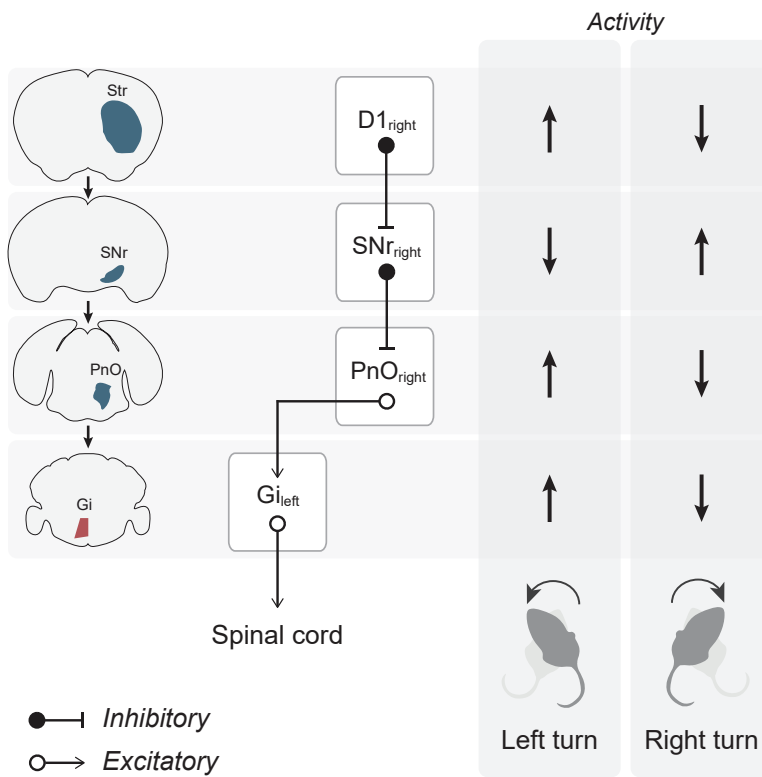


Figure 7. Summary of findings. Activity of D1 SPNs causes contraversive turning gait asymmetries via nigral disinhibition of the PnO → *Chx10* Gi excitatory brainstem-spinal cord pathway (25, 39, 46). Loss of D1 SPN activity causes ipsiversive turning via nigral inhibition of the PnO → *Chx10* Gi excitatory brainstem pathway (25, 40, 54).

tiple excitatory and inhibitory projection neuron subtypes. Uniquely, our study identifies a neuronal pathway from specific SNr neurons that targets a select population of projection neurons within PnO, excitatory neurons which project to the contralateral Gi. This PnO projection subtype exhibits exquisite specificity for limb control, identifying a circuit mechanism for limb-based (body) turning which is recruited by basal ganglia activity (53). The limb-based turning contrasts with the dominant head-based turning evoked by the SNr → SC pathway. Together our data indicate that limb-based turning—which is the major factor determining locomotor direction—and head turning are largely mediated by separate anatomical and functional pathways at the level of SNr and brainstem motor circuits. These data accord with previous work implicating the superior colliculus in the control of head and trunk posture (25, 48, 62, 63). Notably, the SNr → PnO and SNr → SC pathways project ipsilaterally, with the outputs of PnO and SC crossing the midline and re-converging in the contralateral Gi (25, 63). The emergent concept is that mechanisms for body and head direction are organized by parallel circuits within the SNr and brainstem. These circuits may work flexibly in synergy or opposition depending on behavioral need.

Finally, we demonstrate that turning deficits caused by unilateral striatal dopamine depletion can be completely reversed by graded stimulation of the PnO → *Chx10* Gi pathway. From the first experiments using 6-OHDA to mimic dopamine loss after PD (51, 52), it is well established that

unilateral striatal dopamine depletion causes turning towards the lesioned side (52). Although there has been no clear understanding as to how a central dopamine imbalance leads to asymmetric locomotor activity, there is clear evidence of limb-associated changes which drive the action (53). Our study provides a clear basal ganglia-spinal cord pathway mechanism underlying locomotor asymmetries deriving from dopamine imbalance between hemispheres, demonstrating that the asymmetric gait phenotypes arising from such imbalance are mediated predominantly by loss of activity in the excitatory PnO → *Chx10* Gi brainstem-spinal cord pathway (Figure 7). Turning disabilities that are observed in severe PD (29, 33) may readily be explained by decreased activity in the PnO → *Chx10* Gi pathway (Figure 7). Modulation of the PnO → *Chx10* Gi pathway could therefore represent a logical target for deep brain stimulation aimed at alleviating turning disabilities in PD clinically.

Data Availability. Preprocessed behavioral videos, DeepLabCut tracking files, and labeled videos associated with spontaneous turns (Figure 1) and optogenetic experiments (Figures 2, 4-6, Supplementary Figures 2-6) are available at emwr3gev6k. All other data that support the findings of this study are available from the corresponding authors upon reasonable request.

Code Availability. The code used to analyze data and produce figure content associated with kinematic analysis of

spontaneous turns (Figure 1) and optogenetic experiments (Figures 2, 4-6, Supplementary Figures 2-6) are available at emwr3gev6k. Portions of this code were generated with assistance from ChatGPT (GPT-4) by OpenAI. All other code is available from the corresponding authors upon request.

Acknowledgments. We thank K. Sharma, L. Zagoraiou, S. Crone, and T.M. Jessell for the *Chx10^{Cre}* mouse. Imaging was performed in the Core Facility for Integrated Microscopy, Faculty of Health and Medical Sciences, University of Copenhagen. We thank I. Vesth-Hansen, M. Aagaard Andersen, I. Mustafic, and M. Lønstrup for technical and administrative assistance, and members of O.K.’s laboratory for discussion and comments on previous versions of this manuscript. This work was supported by the Lundbeck Foundation (R347-2020-2393) to J.M.C., Neuroscience Academy Denmark to S.K.S., and the European Research Council (ERC) under the European Union’s Horizon 2020 research and innovation program (REP-SCI-693038), the Novo Nordisk Laureate Program (NNF15OC0014186), the Lundbeck Foundation (R276-2018-183 and R345-2020-1769), and the Independent Research Fund Denmark to O.K.

Author contributions. J.M.C. and O.K. conceptualized the study. J.M.C., R.L., and O.K. provided methodology. J.M.C. and S.K.S. carried out the investigations. J.M.C. and O.K. wrote the manuscript. J.M.C. and O.K. supervised the study. J.M.C., S.K.S., and O.K. acquired funds.

Competing interests. The authors declare no competing interests.

REFERENCES

- Jaeon Lee, Wengang Wang, and Bernardo L. Sabatini. Anatomically segregated basal ganglia pathways allow parallel behavioral modulation. *Nature Neuroscience*, 23(11):1388–1398, Nov 2020. ISSN 15461726. doi: 10.1038/s41593-020-00712-5.
- LE McElvain, Y Chen, JD Moore, GS Brigid, BL Bloodgood, BK Lim, RM Costa, and D Kleinfeld. Specific populations of basal ganglia output neurons target distinct brain stem areas while collateralizing throughout the diencephalon. *Neuron*, 109(10):1721–1738.e4, 2021.
- Silvia Arber and Rui M. Costa. Networking brainstem and basal ganglia circuits for movement. *Nature reviews. Neuroscience*, 23(6):342–360, Jun 2022. ISSN 1471-0048. doi: 10.1038/S41583-022-00581-W.
- Tiago Branco and Peter Redgrave. The neural basis of escape behavior in vertebrates. *Annual Review of Neuroscience*, 43:417–439, Jul 2020. ISSN 15454126. doi: 10.1146/annurev-neuro-100219-122527.
- S Grillner and A El Manira. Current principles of motor control, with special reference to vertebrate locomotion. *Physiological reviews*, 100(1):271–320, Jan 2020. ISSN 1522-1210. doi: 10.1152/PHYSREV.00015.2019.
- David Kleinfeld, Martin Deschênes, Fan Wang, and Jeffrey D. Moore. More than a rhythm of life: breathing as a binder of orofacial sensation. *Nature neuroscience*, 17(5):647–651, 2014. ISSN 1546-1726. doi: 10.1038/NN.3693.
- Roberto Leiras, Jared M. Cregg, and Ole Kiehn. Brainstem circuits for locomotion. *Annual review of neuroscience*, 45(1):63–85, Jul 2022. ISSN 1545-4126. doi: 10.1146/ANNUREV-NEURO-082321-025137.
- O. Hikosaka and R. H. Wurtz. Visual and oculomotor functions of monkey substantia nigra pars reticulata. iv. relation of substantia nigra to superior colliculus. *Journal of neurophysiology*, 49(5):1285–1301, 1983. ISSN 0022-3077. doi: 10.1152/JN.1983.49.5.1285.
- Okihide Hikosaka. Basal ganglia mechanisms of reward-oriented eye movement. *Annals of the New York Academy of Sciences*, 1104:229–249, 2007. ISSN 0077-8923. doi: 10.1196/ANNALS.1390.012.
- Jaeon Lee and Bernardo L. Sabatini. Striatal indirect pathway mediates exploration via collicular competition. *Nature*, 599(7886):645–649, Nov 2021. ISSN 1476-4687. doi: 10.1038/S41586-021-04055-4.
- Mark A. Rossi, Haofang E. Li, Dongye Lu, Il Hwan Kim, Ryan A. Bartholomew, Erin Gaidis, Joseph W. Barter, Namsoo Kim, Min Tong Cai, Scott H. Soderling, and Henry H. Yin. A gabaergic nigroretectal pathway for coordination of drinking behavior. *Nature neuroscience*, 19(5):742–748, May 2016. ISSN 1546-1726. doi: 10.1038/NN.4285.
- Kazuya Saitoh, Satoko Hattori, Wen Jie Song, Tadashi Isa, and Kaoru Takakusaki. Nigral gabaergic inhibition upon cholinergic neurons in the rat pedunculopontine tegmental nucleus. *The European journal of neuroscience*, 18(4):879–886, Aug 2003. ISSN 0953-816X. doi: 10.1046/J.1460-9568.2003.02825.X.
- K Takakusaki, T Habaguchi, J Ohtinata-Sugimoto, K Saitoh, and T Sakamoto. Basal ganglia efferents to the brainstem centers controlling postural muscle tone and locomotion: a new concept for understanding motor disorders in basal ganglia dysfunction. *Neuroscience*, 119(1):293–308, Jun 2003. ISSN 0306-4522. doi: 10.1016/S0306-4522(03)00095-2.
- P. Dean, P. Redgrave, and G. W.M. Westby. Event or emergency? two response systems in the mammalian superior colliculus. *Trends in Neurosciences*, 12(4):137–147, 1989. ISSN 01662236. doi: 10.1016/0166-2236(89)90052-0.
- Sten Grillner. Biological pattern generation: the cellular and computational logic of networks in motion. *Neuron*, 52:751–766, Dec 2006. ISSN 08966273. doi: 10.1016/j.neuron.2006.11.008.
- Okihide Hikosaka, Yoriko Takikawa, and Reiko Kawagoe. Role of the basal ganglia in the control of purposive saccadic eye movements. *Physiological reviews*, 80(3):953–978, 2000. ISSN 0031-9333. doi: 10.1152/PHYSREV.2000.80.3.953.
- Andreas Klaus, Joaquim Alves Da Silva, and Rui M. Costa. What, if, and when to move: Basal ganglia circuits and self-paced action initiation. *Annual Review of Neuroscience*, 42:459–483, 2019. ISSN 15454126. doi: 10.1146/annurev-neuro-072116-031033.
- Ariane Ménard, François Auclair, Céline Bourcier-Lucas, Sten Grillner, and Réjean Dubuc. Descending gabaergic projections to the mesencephalic locomotor region in the lamprey petromyzon marinus. *The Journal of comparative neurology*, 501(2):260–273, Jan 2007. ISSN 0021-9967. doi: 10.1002/CNE.21258.
- Junchol Park, Luke T. Coddington, and Joshua T. Dudman. Basal ganglia circuits for action specification. *Annual review of neuroscience*, 43:485–507, Jul 2020. ISSN 1545-4126. doi: 10.1146/ANNUREV-NEURO-070918-050452.
- Martyn Goulding. Circuits controlling vertebrate locomotion: moving in a new direction. *Nature Reviews Neuroscience*, 10(7):507–518, Jul 2009. ISSN 1471-003X. doi: 10.1038/nrn2608.
- Ole Kiehn. Decoding the organization of spinal circuits that control locomotion. *Nature Reviews Neuroscience*, 17(4):224–238, Mar 2016. ISSN 1471-003X. doi: 10.1038/nrn.2016.9.
- Julien Bouvier, Vittorio Caggiano, Roberto Leiras, Vanessa Caldeira, Carmelo Bellardita, Kira Balueva, Andrea Fuchs, and Ole Kiehn. Descending command neurons in the brainstem that halt locomotion. *Cell*, 163(5):1191–1203, Nov 2015. ISSN 00928674. doi: 10.1016/j.cell.2015.10.074.
- V. Caggiano, R. Leiras, H. Goñi-Erro, D. Masini, C. Bellardita, J. Bouvier, V. Caldeira, G. Fisone, and O. Kiehn. Midbrain circuits that set locomotor speed and gait selection. *Nature*, 553(7689):455–460, Jan 2018. ISSN 0028-0836. doi: 10.1038/nature25448.

24. Paolo Capelli, Chiara Pivetta, Maria Soledad Esposito, and Silvia Arber. Locomotor speed control circuits in the caudal brainstem. *Nature*, 551(7680):373–377, Oct 2017. ISSN 0028-0836. doi: 10.1038/nature24064.
25. Jared M. Cregg, Roberto Leiras, Alexia Montalant, Paulina Wanken, Ian R. Wickersham, and Ole Kiehn. Brainstem neurons that command mammalian locomotor asymmetries. *Nature Neuroscience*, 23(6):730–740, Jun 2020. ISSN 15461726. doi: 10.1038/s41593-020-0633-7.
26. D Dautan, A Kovács, T Bayasgalan, MA Diaz-Acevedo, B Pal, and J Mena-Segovia. Modulation of motor behavior by the mesencephalic locomotor region. *Cell reports*, 36(8):109594, Aug 2021. ISSN 2211-1247. doi: 10.1016/J.CELREP.2021.109594.
27. Nicolas Josset, Marie Roussel, Maxime Lemieux, David Lafrance-Zoubga, Ali Rastqar, and Frederic Bretzner. Distinct contributions of mesencephalic locomotor region nuclei to locomotor control in the freely behaving mouse. *Current Biology*, 28(6):884–901.e3, Mar 2018. ISSN 09609828. doi: 10.1016/j.cub.2018.02.007.
28. Giovanni Usseglio, Edwin Gatier, Aurélie Heuzé, Coralie Hérent, and Julien Bouvier. Control of orienting movements and locomotion by projection-defined subsets of brainstem v2a neurons. *Current Biology*, 30(23):4665–4681.e6, Dec 2020. ISSN 18790445. doi: 10.1016/j.cub.2020.09.014.
29. Sophia Hulbert, Ann Ashburn, Lisa Robert, and Geert Verheyden. A narrative review of turning deficits in people with parkinson's disease. *Disability and rehabilitation*, 37(15):1382–1389, 2015. ISSN 1464-5165. doi: 10.3109/09638288.2014.961661.
30. Matthew M. McGregor and Alexandra B. Nelson. Circuit mechanisms of parkinson's disease. *Neuron*, 101(6):1042–1056, Mar 2019. ISSN 1097-4199. doi: 10.1016/J.NEURON.2019.03.004.
31. Anat Mirelman, Paolo Bonato, Richard Camicioli, Terry D. Ellis, Nir Giladi, Jamie L. Hamilton, Chris J. Hass, Jeffrey M. Hausdorff, Elisa Pelosin, and Quincy J. Almeida. Gait impairments in parkinson's disease. *The Lancet. Neurology*, 18(7):697–708, Jul 2019. ISSN 1474-4465. doi: 10.1016/S1474-4422(19)30044-4.
32. Meir Plotnik, Nir Giladi, Yacov Balash, Chava Peretz, and Jeffrey M. Hausdorff. Is freezing of gait in parkinson's disease related to asymmetric motor function? *Annals of neurology*, 57(5):656–663, May 2005. ISSN 0364-5134. doi: 10.1002/ANA.20452.
33. Cris Zampieri, Arash Salarian, Patricia Carlson-Kuhta, Kamiar Aminian, John G. Nutt, and Fay B. Horak. The instrumented timed up and go test: potential outcome measure for disease modifying therapies in parkinson's disease. *Journal of neurology, neurosurgery, and psychiatry*, 81(2):171–176, 2010. ISSN 1468-330X. doi: 10.1136/JNNP.2009.173740.
34. Vrutangkumar V. Shah, James McNames, Martina Mancini, Patricia Carlson-Kuhta, Rebecca I. Spain, John G. Nutt, Mahmoud El-Gohary, Carolin Curtze, and Fay B. Horak. Quantity and quality of gait and turning in people with multiple sclerosis, parkinson's disease and matched controls during daily living. *Journal of neurology*, 267(4):1188–1196, Apr 2020. ISSN 1432-1459. doi: 10.1007/S00415-020-09696-5.
35. P. Crenna, I. Carpinella, M. Rabuffetti, E. Calabrese, P. Mazzoleni, R. Nemni, and M. Ferrarin. The association between impaired turning and normal straight walking in parkinson's disease. *Gait Posture*, 26(2):172–178, Jul 2007. ISSN 0966-6362. doi: 10.1016/J.GAITPOST.2007.04.010.
36. Emma L. Stack, Ann M. Ashburn, and Kate E. Jupp. Strategies used by people with parkinson's disease who report difficulty turning. *Parkinsonism related disorders*, 12(2):87–92, Mar 2006. ISSN 1353-8020. doi: 10.1016/J.PARKRELDIS.2005.08.008.
37. Keith B. J. Franklin and George Paxinos. *Paxinos and Franklin's The mouse brain in stereotaxic coordinates*. ISBN 9780123910578.
38. Li Ju Hsu, Maëlle Bertho, and Ole Kiehn. Deconstructing the modular organization and real-time dynamics of mammalian spinal locomotor networks. *Nature communications*, 14(1), Dec 2023. ISSN 2041-1723. doi: 10.1038/S41467-023-36587-W.
39. Alexxai V. Kravitz, Benjamin S. Freeze, Philip R. L. Parker, Kenneth Kay, Myo T. Thwin, Karl Deisseroth, and Anatol C. Kreitzer. Regulation of parkinsonian motor behaviours by optogenetic control of basal ganglia circuitry. *Nature*, 466(7306):622–626, Jul 2010. doi: 10.1038/nature09159.
40. Fatuel Tecuapetla, Sara Matias, Guillaume P. Dugue, Zachary F. Mainen, and Rui M. Costa. Balanced activity in basal ganglia projection pathways is critical for contraversive movements. *Nature Communications*, 5(1):4315, Dec 2014. ISSN 2041-1723. doi: 10.1038/ncomms5315.
41. Brian Zingg, Xiao-lin Chou, Zheng-gang Zhang, Lukas Mesik, Feixue Liang, Huizhong Whit Tao, and Li I. Zhang. Aav-mediated anterograde transsynaptic tagging: mapping corticocollicular input-defined neural pathways for defense behaviors. *Neuron*, 93(1): 33–47, Jan 2017. ISSN 08966273. doi: 10.1016/j.neuron.2016.11.045.
42. Brian Zingg, Bo Peng, Junxiang Huang, Huizhong W. Tao, and Li I. Zhang. Synaptic specificity and application of anterograde transsynaptic aav for probing neural circuitry. *Journal of Neuroscience*, 40(16):3250–3267, Apr 2020. ISSN 15292401. doi: 10.1523/JNEUROSCI.2158-19.2020.
43. RM Brownstone and JW Chopek. Reticulospinal systems for tuning motor commands. *Frontiers in neural circuits*, 12:30, Apr 2018. ISSN 1662-5110. doi: 10.3389/FNCIR.2018.00030.
44. Lief E. Fenno, Joanna Mattis, Charu Ramakrishnan, Minsuk Hyun, Soo Yeun Lee, Miao He, Jason Tucciarone, Aslihan Selimbeyoglu, Andre Berndt, Logan Grosenick, Kelly A. Zalocusky, Hannah Bernstein, Haley Swanson, Chelsey Perry, Ilka Diester, Frederick M. Boyce, Caroline E. Bass, Rachael Neve, Z. Josh Huang, and Karl Deisseroth. Targeting cells with single vectors using multiple-feature boolean logic. *Nature Methods* 2014 11:7, 11(7):763–772, Jun 2014. ISSN 1548-7105. doi: 10.1038/nmeth.2996.
45. P. Burbaud, B. Bonnet, D. Guehl, A. Lagueny, and B. Bioulac. Movement disorders induced by gamma-aminobutyric agonist and antagonist injections into the internal globus pallidus and substantia nigra pars reticulata of the monkey. *Brain research*, 780(1):102–107, Jan 1998. ISSN 0006-8993. doi: 10.1016/S0006-8993(97)01158-X.
46. Christopher J. Magnus, Peter H. Lee, Jordi Bonaventura, Roland Zemla, Juan L. Gomez, Melissa H. Ramirez, Xing Hu, Adriana Galvan, Jayeeta Basu, Michael Michaelides, and Scott M. Sternson. Ultrapotent chemogenetics for research and potential clinical applications. *Science*, 364(6436), Apr 2019. ISSN 10959203. doi: 10.1126/science.aav5282.
47. Claudio A. Villalobos and Michele A. Basso. Optogenetic activation of the inhibitory nigro-collicular circuit evokes contralateral orienting movements in mice. *Cell reports*, 39(3), Apr 2022. ISSN 2211-1247. doi: 10.1016/J.CELREP.2022.110699.
48. Kaoru Isa, Thongchai Sooksawate, Kenta Kobayashi, Kazuto Kobayashi, Peter Redgrave, and Tadashi Isa. Dissecting the tectal output channels for orienting and defense responses. *eNeuro*, 7(5): 1–18, Sep 2020. ISSN 23732822. doi: 10.1523/ENEURO.0271-20.2020.
49. R. K.W. Schwarting and J. P. Huston. The unilateral 6-hydroxydopamine lesion model in behavioral brain research. analysis of functional deficits, recovery and treatments. *Progress in neurobiology*, 50(2–3):275–331, Oct 1996. ISSN 0301-0082. doi: 10.1016/S0301-0082(96)00040-8.
50. Kim Tieu. A guide to neurotoxic animal models of parkinson's disease. *Cold Spring Harbor Perspectives in Medicine*, 1(1), Sep 2011. ISSN 21571422. doi: 10.1101/CSHPERSPECT.A009316.
51. Urban Ungerstedt. 6-hydroxy-dopamine induced degeneration of central monoamine neurons. *European journal of pharmacology*, 5 (1):107–110, 1968. ISSN 0014-2999. doi: 10.1016/0014-2999(68)90164-7.
52. P. F. Von Voigtlander and K. E. Moore. Turning behavior of mice with unilateral 6-hydroxydopamine lesions in the striatum: effects of apomorphine, l-dopa, amanthadine, amphetamine and other psychomotor stimulants. *Neuropharmacology*, 12(5):451–462, 1973. ISSN 0028-3908. doi: 10.1016/0028-3908(73)90061-0.
53. Gerlinde A. Metz, Arthur Tse, Mark Ballermann, Lori K. Smith, and Karim Fouad. The unilateral 6-ohda rat model of parkinson's dis-

- ease revisited: an electromyographic and behavioural analysis. *The European journal of neuroscience*, 22(3):735–744, Aug 2005. ISSN 0953-816X. doi: 10.1111/j.1460-9568.2005.04238.X.
54. Giorgio Rizzi and Kelly R. Tan. Synergistic nigral output pathways shape movement. *Cell Reports*, 27(7):2184–2198.e4, May 2019. ISSN 22111247. doi: 10.1016/j.celrep.2019.04.068.
 55. Scott S. Bolkan, Iris R. Stone, Lucas Pinto, Zoe C. Ashwood, Jorge M. Iravenda Garcia, Alison L. Herman, Priyanka Singh, Akhil Bandi, Julia Cox, Christopher A. Zimmerman, Jounhong Ryan Cho, Ben Engelhard, Jonathan W. Pillow, and Ilana B. Witten. Opponent control of behavior by dorsomedial striatal pathways depends on task demands and internal state. *Nature neuroscience*, 25(3):345–357, Mar 2022. ISSN 1546-1726. doi: 10.1038/S41593-022-01021-9.
 56. Joanna Schwenkgrub, Evan R. Harrell, Brice Bathellier, and Julien Bouvier. Deep imaging in the brainstem reveals functional heterogeneity in v2a neurons controlling locomotion. *Science Advances*, 6(49):eabc6309, Dec 2020. ISSN 23752548. doi: 10.1126/sciadv.abc6309.
 57. J. M. Deniau, P. Mailly, N. Maurice, and S. Charpier. The pars reticulata of the substantia nigra: a window to basal ganglia output. *Progress in brain research*, 160:151–172, 2007. ISSN 0079-6123. doi: 10.1016/S0079-6123(06)60009-5.
 58. Jeremy F. Atherton and Mark D. Bevan. Ionic mechanisms underlying autonomous action potential generation in the somata and dendrites of gabaergic substantia nigra pars reticulata neurons in vitro. *The Journal of neuroscience: the official journal of the Society for Neuroscience*, 25(36):8272–8281, Sep 2005. ISSN 1529-2401. doi: 10.1523/JNEUROSCI.1475-05.2005.
 59. P. G. Guyenet and G. K. Aghajanian. Antidromic identification of dopaminergic and other output neurons of the rat substantia nigra. *Brain research*, 150(1):69–84, Jul 1978. ISSN 0006-8993. doi: 10.1016/0006-8993(78)90654-6.
 60. H. Nakanishi, H. Kita, and S. T. Kitai. Intracellular study of rat substantia nigra pars reticulata neurons in an *in vitro* slice preparation: electrical membrane properties and response characteristics to subthalamic stimulation. *Brain research*, 437(1):45–55, Dec 1987. ISSN 0006-8993. doi: 10.1016/0006-8993(87)91525-3.
 61. K Takakusaki, R Chiba, T Nozu, and T Okumura. Brainstem control of locomotion and muscle tone with special reference to the role of the mesopontine tegmentum and medullary reticulospinal systems. *Journal of neural transmission (Vienna, Austria: 1996)*, 123(7):695–729, Jul 2016. ISSN 1435-1463. doi: 10.1007/S00702-015-1475-4.
 62. Gidon Felsen and Zachary F. Mainen. Neural substrates of sensory-guided locomotor decisions in the rat superior colliculus. *Neuron*, 60(1):137–148, Oct 2008. ISSN 08966273. doi: 10.1016/j.neuron.2008.09.019.
 63. Sebastian H. Zahler, David E. Taylor, Brennan S. Wright, Joey Y. Wong, Varvara A. Shvareva, Yusol A. Park, and Evan H. Feinberg. Hindbrain modules differentially transform activity of single collicular neurons to coordinate movements. *Cell*, 186(14):3062–3078.e20, Jul 2023. ISSN 1097-4172. doi: 10.1016/J.CELL.2023.05.031.
 64. Eiman Azim, Juan Jiang, Bror Alstermark, and Thomas M. Jessell. Skilled reaching relies on a v2a propriospinal internal copy circuit. *Nature*, 508(7496):357–363, Feb 2014. ISSN 0028-0836. doi: 10.1038/nature13021.
 65. Linda Madisen, Theresa A. Zwingman, Susan M. Sunkin, Seung Wook Oh, Hatim A. Zarifiwala, Hong Gu, Lydia L. Ng, Richard D. Palmiter, Michael J. Hawrylycz, Allan R. Jones, Ed S. Lein, and Hongkui Zeng. A robust and high-throughput cre reporting and characterization system for the whole mouse brain. *Nature neuroscience*, 13(1):133–140, Jan 2010. ISSN 1546-1726. doi: 10.1038/NN.2467.
 66. Hanns Ulrich Zeilhofer, Barbara Studler, Dimitrula Arabadzisz, Claude Schweizer, Seifollah Ahmadi, Beate Layh, Michael R. Bösl, and Jean Marc Fritschy. Glycinergic neurons expressing enhanced green fluorescent protein in bacterial artificial chromosome transgenic mice. *Journal of Comparative Neurology*, 482(2):123–141, Feb 2005. ISSN 00219967. doi: 10.1002/cne.20349.
 67. Carlos Ernesto Restrepo, Line Lundfalld, Gabor Szabó, Ferenc Erdélyi, Hanns Ulrich Zeilhofer, Joel C. Glover, and Ole Kiehn. Transmitter-phenotypes of commissural interneurons in the lumbar spinal cord of newborn mice. *The Journal of comparative neurology*, 517(2):177–192, Nov 2009. ISSN 1096-9861. doi: 10.1002/CNE.22144.
 68. Nobuaki Tamamaki, Yuchio Yanagawa, Ryohei Tomioka, Jun Ichi Miyazaki, Kunihiko Obata, and Takeshi Kaneko. Green fluorescent protein expression and colocalization with calretinin, parvalbumin, and somatostatin in the gad67-gfp knock-in mouse. *The Journal of comparative neurology*, 467(1):60–79, Dec 2003. ISSN 0021-9967. doi: 10.1002/CNE.10905.
 69. Lotta Borgius, C. Ernesto Restrepo, Richardson N. Leao, Noor Saleh, and Ole Kiehn. A transgenic mouse line for molecular genetic analysis of excitatory glutamatergic neurons. *Molecular and Cellular Neuroscience*, 45(3):245–257, Nov 2010. ISSN 10447431. doi: 10.1016/j.mcn.2010.06.016.
 70. M. Hagglund, K. J. Dougherty, L. Borgius, S. Itohara, T. Iwasato, and O. Kiehn. Optogenetic dissection reveals multiple rhythmicogenic modules underlying locomotion. *Proceedings of the National Academy of Sciences*, 110:11589–11594, Jul 2013. ISSN 0027-8424. doi: 10.1073/pnas.1304365110.
 71. Linh Vong, Chianping Ye, Zongfang Yang, Brian Choi, Streamson Chua, and Bradford B. Lowell. Leptin action on gabaergic neurons prevents obesity and reduces inhibitory tone to pomc neurons. *Neuron*, 71(1):142–154, Jul 2011. doi: 10.1016/j.neuron.2011.05.028.
 72. D. Gowanlock R. Tervo, Bum Yeol Hwang, Sarada Viswanathan, Thomas Gaj, Maria Lavzin, Kimberly D. Ritola, Sarah Lindo, Susan Michael, Elena Kuleshova, David Ojala, Cheng Chiu Huang, Charles R. Gerfen, Jackie Schiller, Joshua T. Dudman, Adam W. Hantman, Loren L. Looger, David V. Schaffer, and Alla Y. Karpova. A designer aav variant permits efficient retrograde access to projection neurons. *Neuron*, 92(2):372–382, Oct 2016. ISSN 10974199. doi: 10.1016/j.neuron.2016.09.021.
 73. M Mahn, L Gibor, P P. Patil, K K. Cohen-Kashi Malina, S Oring, Y Printz, R Levy, I Lampl, and O Yizhar. High-efficiency optogenetic silencing with soma-targeted anion-conducting channelrhodopsins. *Nature communications*, 9(1), Dec 2018. ISSN 2041-1723. doi: 10.1038/S41467-018-06511-8.
 74. Alexander Mathis, Pranav Mamidanna, Kevin M. Cury, Taiga Abe, Venkatesh N. Murthy, Mackenzie Weygandt Mathis, and Matthias Bethge. DeepLabCut: markerless pose estimation of user-defined body parts with deep learning. *Nature Neuroscience*, 21(9):1281–1289, Sep 2018. ISSN 1097-6256. doi: 10.1038/s41593-018-0209-y.
 75. Tanmay Nath, Alexander Mathis, An Chi Chen, Amir Patel, Matthias Bethge, and Mackenzie Weygandt Mathis. Using deepLabCut for 3d markerless pose estimation across species and behaviors. *Nature Protocols*, 14(7):2152–2176, Jul 2019. ISSN 1754-2189. doi: 10.1038/s41596-019-0176-0.
 76. Jeffrey E. Markowitz, Winthrop F. Gillis, Celia C. Beron, Shay Q. Neufeld, Keiramarie Robertson, Neha D. Bhagat, Ralph E. Peterson, Emalee Peterson, Minsuk Hyun, Scott W. Linderman, Bernardo L. Sabatini, and Sandeep Robert Datta. The striatum organizes 3d behavior via moment-to-moment action selection. *Cell*, 174(1):44–58.e17, Jun 2018. ISSN 1097-4172. doi: 10.1016/J.CELL.2018.04.019.
 77. Caroline A. Schneider, Wayne S. Rasband, and Kevin W. Eliceiri. NIH image to ImageJ: 25 years of image analysis. *Nature methods*, 9(7):671–675, Jul 2012. ISSN 1548-7105. doi: 10.1038/NMETH.2089.
 78. Dominic A. Evans, A. Vanessa Stempel, Ruben Vale, Sabine Ruehle, Yaara Leffler, and Tiago Branco. A synaptic threshold mechanism for computing escape decisions. *Nature*, 558 (7711):590–594, Jun 2018. ISSN 14764687. doi: 10.1038/s41586-018-0244-6.
 79. Joshua H. Jennings, Christina K. Kim, James H. Marshel, Misha

Raffiee, Li Ye, Sean Quirin, Sally Pak, Charu Ramakrishnan, and Karl Deisseroth. Interacting neural ensembles in orbitofrontal cortex for social and feeding behaviour. *Nature*, 565(7741):645–649, Jan 2019. ISSN 14764687. doi: 10.1038/s41586-018-0866-8.

MATERIALS AND METHODS

Mice.

Animal procedures were performed in accordance with European Union Directive 2010/63/EU, and approved by the Danish Animal Inspectorate (Dyreforsøgstilsynet, permit 2017-15-0201-01172) as well as the local ethics committee at the University of Copenhagen (permit P21-323). The following mouse strains were used for the experiments herein: *Chx10*^{Cre} (64), *D1*^{Cre} (Gensat EY217), *D2*^{Cre} (Gensat ER44), *R26R*^{LSL-tdTom} (65) (Ai14, Jackson Stock #007914), *WT* (C57BL6/J, Jackson Stock #000664), *GlyT2*^{GFP} (66), *Gad67*^{GFP} (67, 68), *Vglut2*^{Cre} (69), *Vgat*^{Cre} (70) or (71) (Jackson Stock#028862). Mice were housed in ventilated cages with ad libitum access to food and water. Cages were maintained within a temperature (23-24 °C) and humidity (45-50%) controlled environment, with a 12 hr light/dark cycle. Experiments were performed in adult mice greater than 8 weeks of age, with an effort to include similar numbers of male and female mice.

Stereotaxic viral injections.

Anesthesia was induced with 4% isofluorane (Link 7 Anesthesia & Evacuation System, Patterson Scientific), and then maintained at 1.5-2% during surgery. Mice were secured to a stereotaxic frame (Model 900, David Kopf Instruments) which was driven by a robotic controller (Neurostar). Mice were kept on a 37 °C heating pad (Rodent Warmer X1, Stoelting) for the duration of the surgery. Viscotears were applied to the eyes to prevent dehydration. The skin on the head was shaved, and an incision was made to expose the skull. Skull references were taken for bregma and lambda, and a small burr hole was drilled in the skull overlying the target brain region for injection. The underlying dura was opened. A pulled glass capillary was filled with mineral oil and secured to a capillary nanoinjector (Neurostar). Viruses were mixed with a small amount of fast green for visualization and loaded into the capillary. The capillary was advanced to the target brain region at a rate of 0.1 mm s⁻¹, and injections were performed at a rate of 100 nl min⁻¹. The capillary was left in place for 5 min following the injection and then withdrawn at a rate of 0.1 mm s⁻¹. The skin was closed using a series of individual 6-0 sutures (Ethicon) or wound clips (7 mm, Reflex Autoclip System). Mice were allowed to recover on the heating pad, and post-operative buprenorphine (0.3 mg kg⁻¹) was given for pain management.

For Ca²⁺ recording from *Chx10* Gi neurons (Figures 1, 2, Supplementary Figures 1, 2), AAV1-hSyn1-DIO-GCaMP6s (for endoscopic imaging; 100845-AAV1, 2.0 x 10¹³ ml⁻¹, Addgene) or AAV9-hSyn1-DIO-GCaMP7s (for fiber photometry; v407-9, 5.0 x 10¹² ml⁻¹, Viral Vector Facility, University of Zurich) was injected in *Gi*_{left} (coordinates: -6.0 mm anteroposterior, AP, -0.8 mm mediolateral, ML, -5.5 mm dorsoventral, DV). The coordinates for injection in *Gi* are the same as those used in refs. (22, 25, 28). Ca²⁺ recordings were combined with optogenetic stimulation of direct or indirect pathway striatal projection neurons in *D1*^{Cre}; *Chx10*^{Cre} or *D2*^{Cre}, *Chx10*^{Cre} dual-allelic mice (Figure 2, Supplementary Figures 1, 2, 3). We targeted the dorsomedial striatum based on previous data indicating that turning is most effectively induced by stimulation of the medial sector (1), comparable with ref. (39), although turning can also be evoked from the dorsolateral striatum (1, 40). For this, AAVdj-Ef1a-DIO-hChR2(E123T/T159C)-p2A-mCherry-WPRE (GVVC-AAV-33, 9.0 x 10¹² ml⁻¹, AAV Stanford) was injected bilaterally in the dorsomedial striatum (coordinates: +0.5 mm AP, ±1.5 mm ML, -3.5 mm DV).

For the intersectional strategy targeting PnO neurons (Figures 3, 4, 6, Supplementary Figures 4, 6), 350 nl of Cre-, FlpO-, or Cre/FlpO (con/fon)-dependent retrograde AAV virus (72) was injected in *Gi*_{left} in *WT*, *Gad67*^{GFP}, *GlyT2*^{GFP}, or *Vglut2*^{Cre} mice. The following AAV_{retro} viruses were used for these experiments: AAV_{retro}-hSyn1-fDIO-ChrimsonR-tdTom (v413-retro, 4.4 x 10¹² ml⁻¹, Viral Vector Facility, University of Zurich), AAV_{retro}-Ef1a-DIO-hChR2(H134R)-EYFP (20298-AAVrg, 1.0 x 10¹³ ml⁻¹, Addgene), AAV_{retro}-hSyn1-DIO-GtACR2-EGFP (v477-retro, 7.3 x 10¹² ml⁻¹, Viral Vector Facility, University of Zurich), AAV_{retro}-hSyn1-fDIO-EGFP-2A-TeLC (v450-retro, 7.7 x 10¹² ml⁻¹, Viral Vector Facility, University of Zurich), or AAV_{retro}-hSyn1-con/fon-hChR2(H134R)-EYFP (55645-AAVrg, 7.0 x 10¹² ml⁻¹, Addgene). The injection of AAV_{retro} in *Gi* was followed 1 week later by injection of 100 nl of AAV1-hSyn1-FlpO (v59-1, 6.7 x 10¹² ml⁻¹, Viral Vector Facility, University of Zurich) or AAV1-hSyn1-Cre (v223-1, 5.2 x 10¹² ml⁻¹, Viral Vector Facility, University of Zurich) in SNr_{right} (coordinates: -3.2 mm AP, +1.20 mm ML, -4.9 mm DV). Injections in SNr were performed at an angle of -15° in the coronal plane to avoid the superior colliculus.

For the intersectional strategy targeting *Chx10* Gi neurons (Supplementary Figure 4), *Chx10*^{Cre} mice were injected with 400 nl of AAV5-hSyn1-con/fon-hChR2(H134R)-EYFP (55645-AAV5, 7.0 x 10¹² ml⁻¹, Addgene) in *Gi*_{left} (coordinates: -6.0 mm AP, -0.8 mm ML, -5.5 mm DV) followed 1 week later by injection of 80 nl of AAV1-hSyn1-FlpO (v59-1, 6.7 x 10¹² ml⁻¹, Viral Vector Facility, University of Zurich) in PnO_{right} (coordinates: -4.3 mm AP, +0.80 mm ML, -4.8 mm DV).

For experiments targeting SNr (Figure 5, Supplementary Figure 5), 100 nl of Cre-dependent AAV virus was injected in SNr_{right} (coordinates: -3.2 mm AP, +1.15 mm ML, -4.9 mm DV) of *Vgat*^{Cre} mice. The following viruses were used: AAV5-hSyn1-DIO-GtACR2-EGFP (v477-5, 7 x 10¹² ml⁻¹, Viral Vector Facility, University of Zurich), or AAVdj-Ef1a-DIO-hChR2(E123T/T159C)-p2A-mCherry-WPRE (GVVC-AAV-33, 9 x 10¹² ml⁻¹, AAV Stanford). For retrograde experiments targeting SNr from PnO or superior colliculus, 80 nl of AAV_{retro} virus was injected in PnO_{right} (coordinates: -4.3 mm AP, +0.80

mm ML, -4.8 mm DV) or SC_{right} (coordinates: -4.25 mm AP, +1.10 mm ML, -1.8 mm DV) in *Vgat*^{Cre} mice. The following viruses were used: AAV_{retro}-hSyn1-DIO-GtACR2-EGFP (v477-retro, 7.3 x 10¹² ml⁻¹, Viral Vector Facility, University of Zurich), or AAV_{retro}-Ef1a-DIO-hChR2(H134R)-EYFP (20298-AAVrg, 1 x 10¹³ ml⁻¹, Addgene).

For chemogenetic activation of *Chx10* Gi neurons (Figure 6, Supplementary Figure 6), 400 nl of AAV5-hSyn1-DIO-hM3D(Gq)-mCherry-WPRE (v89-5, 6 x 10¹² ml⁻¹, Viral Vector Facility, University of Zurich) was injected into Gi_{left} (coordinates: -6.0 mm AP, -0.8 mm ML, -5.5 mm DV) in *Chx10*^{Cre} mice.

Endoscopic Ca²⁺ imaging.

Similar surgical procedures as above (Stereotaxic viral injections) were used for GRIN lens implantation. Integrated GRIN lenses (7.3 mm length, 0.6 mm diameter, Inscopix) were modified to image in the Gi. Flexible piano wire (100 μm diameter, SMWL-004-01, Precision Fiber Optics) was cut to 5 mm length. Loctite adhesive was used to attach two 5 mm wires to the GRIN lens at 180° separation, leaving 0.5 mm wire protruding from the brain-directed surface of the lens. The protruding wire thus stabilized the underlying brain tissue, which helped to reduce motion artifact during image acquisition. GRIN lens implantation in Gi was performed following bilateral optogenetic fiber implantation in striatum (below, Optogenetics). Optogenetic fibers were implanted at ± 15° in the coronal plane, preserving access to bregma for reference with a pre-track needle and naked GRIN lens. To make space for the GRIN lens, a tissue track was created with a 23-gauge needle advanced toward Gi at a rate of 0.01 mm s⁻¹. The pre-track needle was withdrawn upon reaching a DV position of -5.0 mm. A wire-attached GRIN lens was then driven to Gi at a rate of 0.01 mm s⁻¹, with final coordinates of -6.0 mm AP, -0.35 mm ML, -5.3 mm DV. The integrated GRIN lens/baseplate was then cemented to the skull using Super Bond C&B (7100, Sun Medical Co.). To reduce ambient light, the Super Bond C&B cement powder was mixed with black carbon powder at a ratio of 10:1.

Endoscopic imaging was performed with an nVoke 2.0 miniature microscope (Inscopix), which was mounted on the integrated GRIN lens/base plate. A commutator system (Inscopix) was used to minimize cable entanglement. Imaging was performed > 3 weeks after implantation following tissue debridement and substantial clearance of the field of view. Electronic focusing was used to determine the optimal field-of-view, which was maintained for individual mice across imaging sessions. Images were acquired at a rate of 20 Hz with 30-50% LED power, and 2-4x gain. Inscopix data was synchronized with behavioral videos via a TTL pulse passed to the Inscopix DAQ box by Ethovision XT (v15.0, Noldus). Recordings varied in length between 1-10 minutes. While the procedures for endoscopic imaging were similar to those in (56), we obtained a much smaller yield, and in many animals (not included in this study) we observed no dynamic cells. We have no explanation for these differences. To facilitate future replication and comparisons with the Gi recordings presented herein, we adopted a quantitative definition of cells; *bona fide* cells were defined as ROIs which exhibited greater than 3.5% dF/F over 3 minutes of recording. dF/F ranged between 4.0-17.0%, with an average dF/F of 7.4 ± 1.3% (*n* = 7 cells).

Fiber photometry.

Similar surgical procedures as above (Stereotaxic viral injections) were used for fiberoptic cannula implantation. Custom borosilicate fiberoptic cannulas were obtained from Doric Lenses (400 μm diameter, NA = 0.66, MFC_400/430-0.66_3-0-6.0mm_MF1.25_FLT), attached to a stereotaxic cannula holder (Doric Lenses, SCH_1.25), and driven to the target brain region at a rate of 0.1 mm s⁻¹. For optic fiber placement, the skull was prepared using a two-component adhesive (Optibond FL, Kerr). Dental cement (Tetric EvoFlow Bulk Fill, Ivoclar Vivadent) was applied around the ferrule, and cured with UV light (Superlite 1300, M+W Dental) to affix the implant to the surface of the skull. The cannula holder was then loosened and withdrawn, and individual 6-0 sutures were used to close the skin surrounding the implant. The following fiber coordinates were used: Gi_{left}, -6.0 mm AP, -0.35 mm ML, -5.3 mm DV.

Fiber photometry was performed using a RZ10X processor (Tucker-Davis Technologies). 465 nm (for GCaMP excitation) and 405 nm (for isosbestic excitation) LEDs were driven at modulated frequencies, where isosbestic excitation serves as an internal control for photobleaching and movement artifacts. LEDs were driven at a power of 10 mA (peak-to-peak, with 5 mA DC offset), and modulated at 330 Hz (465 nm) and 210 Hz (405 nm). LEDs were coupled to a fluorescence minicube (FMC4_IE(400-410)_E(460-490)_F(500-550)_S, Doric Lenses), which passed 405/465 nm excitation light to the subject via a patch cord (Tucker-Davis Technologies), rotary joint (FRJ_1x1_PT_400-0.57_1m_FCM_0.15m_FCM, Doric Lenses), and subject cable (MFP_400/430/1100-0.57_1m_FCM-MF1.25_LAF, Doric Lenses). Emitted light was filtered via the minicube (500-550 nm) and passed back to an integrated photosensor on the RZ10X processor. Data was acquired in Synapse (Tucker-Davis Technologies), which demodulated the 405 and 465 nm signals. Synapse data was synchronized with behavioral videos via a TTL pulse passed to the RZ10X processor by Ethovision XT. Recordings varied in length between 1-10 minutes.

Optogenetics.

Silica optic fiber (200 μm core, NA = 0.22, FG200UEA, Thorlabs) was cut to 5 cm, and a micro stripper (T10S13, Thorlabs) was used to strip the acrylate coating on 1.5 cm of the fiber used for mating with a ferrule. Ceramic ferrules (6.7 mm, CFLC230-10, Thorlabs) were then placed on the stripped portion of the optic fiber, and secured using epoxy (F112, Thorlabs). After the

epoxy was allowed to dry for 7 days, the stripped fiber was trimmed to a length of 1 mm from the upper surface of the ferrule using an optic fiber scribe (S90R, Thorlabs). A coarse piece of polishing paper (LF5P, Thorlabs) was then used to reduce the protruding fiber to the upper surface of the ferrule on a glass polishing plate (CTG913, Thorlabs), and a finer series of paper (LF3P, LF1P, LF03P, Thorlabs) was used to polish the optic fiber. The fiber optic scribe was then used to cut the remaining optic fiber with acrylate coating to a length approximately 0.5 mm longer than the final target depth (which varied depending on the target brain region). Similar surgical procedures as above (Stereotaxic viral injections and Fiber photometry) were used for optic fiber implantation. The following fiber coordinates were used: Gi, -6.0 mm AP, -0.35 mm ML, -5.1 mm DV; PnO, -4.3 mm AP, +0.8 mm ML, -4.3 mm DV; SNr, -3.2 mm AP, +1.15 mm ML, -4.3 mm DV; striatum, +0.5 mm AP, ±1.5 mm ML, -2.8 mm DV.

For delivery of light pulses, Ethovision XT was used to trigger a Master-8 pulse generator (AMPI) via a TTL pulse. For ChR2 experiments, the Master-8 was used to generate a 1 s train. Experiments in Figures 1, 2 and Supplementary Figures 2-4 utilized a 40 Hz train (15 ms pulse width, 10 ms interval between pulses). For experiments in Figures 4, 6, Supplementary Figure 6, stimulation frequency was varied between 5-40 Hz while keeping laser power and pulse width constant: 5 Hz (15 ms pulse width, 185 ms interval), 10 Hz (15 ms pulse width, 85 ms interval), 20 Hz (15 ms pulse width, 35 ms interval), 40 Hz (15 ms pulse width, 10 ms interval). For GtACR2 experiments, the Master-8 was used to generate a 1 s continuous pulse. The Master-8 triggered a 473 nm laser (Laserglow Technologies), which delivered light via a patch cable (M74L01, Thorlabs), rotary joint (RJ1, Thorlabs), and optic fiber cable (FG105UCA, Thorlabs) to the optic fiber-ferrule implant. Pseudo-random optogenetic stimulation was triggered while mice were moving through the center of the arena. In 2 of 9 mice with GtACR2 expression in PnO-Vglut₂_{contra} neurons (Figures 4I-K), GtACR2 initiated a short-lasting left (contralateral) turn immediately followed by a prolonged right (ipsilateral) turn. This behavior is consistent with early spiking caused by GtACR2 followed by prolonged neuronal inhibition (73).

Open field behavior.

Open-field behavioral analysis was performed in custom-fabricated 50 x 50 cm arenas. Testing in the spiral maze (Figures 4L-N) was carried out as described previously (25). Briefly, mice were placed in the center of the maze, and allowed to explore the maze to completion or until 10 min had elapsed. For optogenetics in 6-OHDA lesioned mice (Figure 6, Supplementary Figure 6), mice were tested in a 15 cm diameter cylinder, which promotes locomotor turning (25). Behavior was captured using an overhead camera (25 f.p.s., 1280 x 960 square pixels, acA1300-60gm camera, Basler; H3Z4512CS-IR lens, Computar), and recorded using Ethovision XT. For chemogenetics in 6-OHDA lesioned mice (Figure 6 and Supplementary Figure 6), open field behavior was captured in four 50 x 50 cm arenas imaged simultaneously using a bottom view camera (30 f.p.s., GO-5000M-USB camera, JAI; LM12HC lens, Kowa Optical Products), and recorded in eBUS player (Pleora Technologies).

6-OHDA lesions.

Thirty minutes prior to unilateral 6-OHDA injection, mice received an intraperitoneal injection of desipramine (25 mg kg⁻¹) to prevent 6-OHDA damage to the noradrenergic system. One μ l of 6-OHDA (5 mg ml⁻¹ dissolved in a 0.2% ascorbic acid/saline solution) was injected unilaterally into the right dorsomedial striatum (DMS) as above (Stereotaxic viral injections). The injection was performed at the following coordinates: +0.5 mm AP, +1.5 mm ML, -3.5 mm DV.

To improve recovery after 6-OHDA lesion, supplemental nutrition including wet chow pellets, condensed milk, and Nutella was given daily. Supplemental nutrition was provided one week prior to 6-OHDA lesion to prevent food neophobia and was discontinued upon recovery from the lesion. 6-OHDA lesioned mice were assessed daily for weight loss and dehydration within the first 10 days post-lesion, and thereafter every two days. Dehydrated mice received fluids (either saline or 5% glucose), and hypothermic mice were warmed by placing their cage on a heating pad. Mice were euthanized if they exhibited greater than 15% weight loss.

Chemogenetics.

CNO (4936, Tocris) was dissolved in 0.9% saline at a concentration of 0.1 mg ml⁻¹. Saline or CNO (1 mg kg⁻¹) was then administered intraperitoneally, and mice were placed in an open field arena. Open field behavior was recorded for 40 minutes.

Immunocytochemistry and *in situ* hybridization.

For immunocytochemistry, mice were administered an anesthetic overdose of pentobarbital (250 mg kg⁻¹). Transcardial perfusion was subsequently performed with 4 °C phosphate buffered saline (PBS) followed by 4% paraformaldehyde in 0.1 M phosphate buffer (HL96753.1000, HistoLab). Brain tissue was dissected free and post-fixed for 3 h in 4% paraformaldehyde at 4 °C. The tissue was transferred to 27.5% sucrose dissolved in phosphate buffered saline for cryoprotection and incubated at 4 °C for 24-48 h. Tissue was washed with PBS to remove excess sucrose, pat dry, and embedded in NEG-50 medium (D22267, ThermoFisher Scientific). Tissue blocks were then frozen on dry ice and stored at -20 °C. Frozen coronal or sagittal sections (30-50 μ m) were obtained on a cryostat (CryoStar NX70, ThermoScientific), and mounted on slides (Superfrost Plus, ThermoScientific).

Sections were rehydrated in PBS with 0.5% triton-X100 (PBS-T; X100, SigmaAldrich) for 5 min, and then blocked with PBS-T + 10% normal donkey serum (Jackson ImmunoResearch) for 2 h at room temperature. Sections were incubated in primary antibodies diluted in blocking solution overnight at 4 °C. The following primary antibodies were used: rabbit anti-dsRed/mCherry/tdTomato (1:1000, 632496, Takahara Bio), chicken anti-GFP (1:1000, ab13970, Abcam), rabbit anti-TH (1:1500, AB152, Millipore). Slides were washed 4 x 10 min in PBS-T and incubated with appropriate Alexa 488- or Alexa 568-conjugated secondary antibodies (1:500, ThermoFisher Scientific) diluted in blocking solution. Counterstaining was performed with Hoechst 33342 (1:2000, 62249, ThermoFisher Scientific) or NeuroTrace 435 (1:200, N21479, ThermoFisher Scientific). Coverslips were mounted using mowiol 4-88 mounting medium (475904-M, Sigma Aldrich). Images were acquired using a Zeiss LSM 900.

For *in situ* hybridization, mice were administered an anesthetic overdose of pentobarbital, and transcardial perfusion was performed with 4 °C phosphate buffered saline (PBS). Brain tissue was rapidly dissected free and flash-frozen in isopentane cooled on dry ice. Tissue was then embedded in NEG-50 medium and stored at -80 °C prior to cutting. Cryosections (14 µm) were mounted and stored at -80 °C prior to hybridization. *In situ* hybridization for target genes was performed using the RNAscope Multiplex Fluorescent Assay v2 (323110, Advanced Cell Diagnostics, ACD) using the following RNAscope Target Probes (ACD): *tdTom* (317041-C3), *Slc17a6* (*Vglut2*, 319171-C2), *Slc32a1* (*Vgat*, 319191-C1). Individual channels were developed using Opal 520, 570, and 690 dyes (1:1500, Akoya Biosciences). Sections were counterstained with DAPI, and coverslips were mounted with ProLong Diamond Antifade (P36961, ThermoFisher Scientific) medium. Images were acquired using a Zeiss LSM 900.

Analysis.

Behavioral tracking

Behavioral tracking was performed offline using DeepLabCut (74, 75). DeepLabCut v.2.0 was installed on a PC equipped with a GEFORCE RTX2080 graphics card. Videos were downsampled to a resolution of 640 x 480 square pixels prior to analysis. An initial training dataset was assembled from approximately 400 frames extracted from videos representing different mice, behavioral sessions, and behavioral paradigms; frames were extracted from videos of mice with no cable, an optogenetic cable, a miniscope, a miniscope and optogenetic cable, a fiber photometry cable, and both a fiber photometry and optogenetic cable. Frames in the training dataset were manually labeled for the tip of the nose, neck, body center, tail base, and tail tip. A resnet50 network was trained for 1 x 10⁶ iterations on the initial training dataset. Videos representative of different behavioral paradigms were then analyzed using the resnet50 network, and outlier frames were extracted. Outlier frames were scored and merged with the initial training dataset to assemble a modified training dataset. A resnet50 network was generated using the modified training dataset, and this network was used for subsequent analyses. For chemogenetic experiments (Figure 6, Supplementary Figure 6), behavioral tracking was performed offline in Ethovision XT, which extracted nose, body center, and tail base position.

Kinematics

The following kinematic variables were derived using custom scripts in MATLAB (version R2021a, MathWorks) from x,y position data generated by DeepLabCut: direction, angular velocity, speed, and turn radius. For Figures 1, 2, 6, Supplementary Figures 2, 6, direction was calculated from the body-snout vector. For Figures 4, 5, Supplementary Figures 3, 4, 5, direction was calculated separately for the body (body-neck vector) and the head relative to the body (head; direction of the neck-head vector – direction of the body vector):

$$\theta = \tan^{-1} \frac{y_2 - y_1}{x_2 - x_1}$$

where θ is direction in degrees. Phase unwrapping of the θ_t time series was used to represent changes in direction continuously through a four-quadrant space. For Figure 4E, each trial was adjusted such that direction was equal to 0 at light onset. Angular velocity data was then calculated from θ_t , with a bin of 80 ms (representing 3 frames):

$$av_t = \frac{\theta_{t+1} - \theta_{t-1}}{0.08}$$

where av is the angular velocity in ° s⁻¹. Positive angular velocity represents counterclockwise (left) movement, and negative angular velocity represents clockwise (right) movement. Speed was calculated from the body position, converting pixel size to cm, with a bin of 80 ms:

$$v_t = \frac{\sqrt{(x_{t+1} - x_{t-1})^2 + (y_{t+1} - y_{t-1})^2}}{0.08}$$

where v is the speed in cm s⁻¹. Turning radius was approximated from v_t and av_t , converting angular velocity to radians s⁻¹:

$$r_t = \frac{v_t}{av_t}$$

where r is the turning radius in cm.

For Figures 6D-F, Supplementary Figures 6B-F, revolution analysis was performed in Ethovision XT, where 360° left (counterclockwise) and right (clockwise) revolutions were quantified using the tail base to body center vector, with a 50° threshold for switching between measurement of left and right revolutions. For continuous measurement of leftward movement preference (Figure 6E, Supplementary Figures 6B,E), left revolutions were quantified as a percentage of the total number of revolutions in 5 minute bins. If no revolutions were recorded during a 5 minute bin, left preference was reported as 50%. For box and whisker plots (Figures 6D,F, Supplementary Figures 6C,D,F), revolutions were quantified from 10-40 minutes after injection of saline or CNO.

Ca²⁺ analysis

Post-processing of endoscopic imaging data was performed in Inscopix Data Processing software (IDPS v1.6.0, Inscopix). Inscopix (.isdx) files were imported into IDPS and underwent preprocessing to crop the field of view and downsample spatial resolution (2x). Spatial filtering was performed with low (0.005 pixel⁻¹) and high (0.5 pixel⁻¹) pass Gaussian filters, and motion correction was performed using a ROI which contained the imaging field. *dF/F* was defined relative to the mean frame (F_0). Manual ROIs were used to register putative cells, and bona fide cells were defined as ROIs which exhibited greater than 3.5% *dF/F*. *dF/F* ranged between 4.0-17.0%, with an average *dF/F* of 7.4 ± 1.3 ($n = 7$ cells).

Post-processing of fiber-photometry data was performed in Spike2 (Cambridge Electronic Design). Synapse files (.TSQ) were imported into Spike2, and the fluorescence signal (F_t) was defined as the difference between the 465 nm and 405 nm channels (GCaMP excitation – isosbestic excitation). The signal was smoothed using a low pass digital finite impulse response (FIR) filter and linearly downsampled to 25 Hz. *dF/F* was defined relative to the mean fluorescence of the trace (F_0); *dF/F* was defined as $(F_t - F_0) / F_0$. GCaMP7s signal quality was evaluated, and animals which exhibited greater than 10% *dF/F* were selected for further analysis. *dF/F* ranged between 13-73%, with an average *dF/F* of $41 \pm 5\%$ ($n = 14$ mice).

For analysis of *dF/F* activity during spontaneous left or right turns and ChR2-stimulation trials (Figures 1D,E, 2C,D, Supplementary Figure 2B), row *dF/F* z-score was calculated for each event/trial to scale for the difference in magnitude of *dF/F* activity exhibited across cells (for endoscopic imaging) or animals (for fiber photometry). Row Z-scores were calculated based on the mean and standard deviation of *dF/F* values during the baseline period (time -2.5 to 0 s).

Cross-correlation

To evaluate the correlation between GCaMP fluorescence and behavior (Figure 1C), we performed cross correlation between the angular velocity (*av*) and the derivative of the *dF/F* (*ddF/F*) time series (76). Cross-correlation was performed using a custom MATLAB script:

$$[CC, lags] = crosscorr(av, dFF, 400)$$

where *CC* is the cross-correlation calculated with a maximum lag of 400 frames (20 s). Cross-correlation analysis was performed using 3 min of recording in the absence of ChR2 stimulation.

Segmentation of spontaneous turns

Spontaneous left turns, straight events, and right turns (Figures 1D,E, Supplementary Video 2) were segmented from *av_t* using a custom MATLAB script. Left turns were defined as an angular velocity greater than 200 ° s⁻¹ within 1 s of 0 ° s⁻¹. Straight events were defined as an angular velocity that remained between ± 20 ° s⁻¹ for 1 s. Right turns were defined as an angular velocity less than -200 ° s⁻¹ within 1 s of 0 ° s⁻¹. Event onset was considered 0 ° s⁻¹. For endoscopic imaging, the first 20 left turns, 20 straight events, and 20 right turns were quantified for each animal. For fiber photometry, the first 10 left turns, 10 straight events, and 10 right turns were quantified for each animal.

Co-expression

Analysis of neuronal co-expression of *tdTom*, *Vglut2*, and *Vgat* in Figure 3C was carried out in ImageJ (77) using the ROI 1-Click Tools plugin. Neurons were considered *tdTom*⁺ if they exhibited at least 4 positive puncta in close association with a DAPI-labeled nucleus. $98.4 \pm 0.5\%$ ($n = 4$ mice) of *tdTom*⁺ neurons exhibited co-expression of either *Vglut2* or *Vgat*. $1.6 \pm 0.5\%$ were not assigned as *tdTom*⁺*Vglut2*⁺ or *tdTom*⁺*Vgat*⁺ due to putative co-expression of both *Vglut2* and *Vgat* or a lack of either *Vglut2* or *Vgat* co-expression. Similar analysis was performed to assess co-expression of *tdTom* and GFP in Figure 3D.

Atlas registration

Atlas registration of PnO-Vglut2_{contra} neurons in Figure 3E was performed by manually assigning sections to corresponding coronal plates in Paxinos and Franklin's reference atlas (37). Neuronal position within each image was manually registered using ImageJ, converting pixel size to μm. A landmark reference at 0.0 mm ML, -1.25 mm DV was used to transform coordinates onto the reference atlas. Sections were quantified every 100 μm through the rostrocaudal extent of PnO, with 11-14 sections quantified for each mouse. An average of 188 ± 34 neurons were registered for each mouse ($n = 3$ mice).

Statistics.

Mouse Cohorts

Sample sizes are similar to those reported previously (23, 25, 78, 79); no formal statistical methods were used to pre-determine sample size. A block design was used to randomly allocate mice to different groups, with an effort to include both males and females in each group (sex for each experiment is reported in Supplementary Table 1). Sex-specific responses were examined post hoc for those experiments with equivalent numbers of males and females; however, no evidence for sexually dimorphic responses was uncovered.

Blinding

Data collection and analysis were not blinded to the experimenter; however, data collection and analysis were automated to limit the influence of the experimenter on outcome.

Exclusion Criteria

For endoscopic imaging (Figures 1, 2), ROIs which exhibited less than 3.5% dF/F were excluded from analysis. Additionally, mice were excluded on the basis of lens movement artifact, lack of cells, or poor field of view. For fiber photometry (Figures 1, 2, Supplementary Figure 2), mice which exhibited less than 10% dF/F were excluded from analysis. Additionally, mice were excluded based on the stability of the isosbestic control signal; an unstable isosbestic signal is indicative of fiber movement artifact. For optogenetics (Figures 2, 4, 5, 6, Supplementary Figures 2-6), mice were excluded from analysis if the fiber position or viral infection was off target. For chemogenetics (Figure 6, Supplementary Figure 6), mice were excluded from analysis if the viral infection exhibited substantial spread across the midline. For 6-OHDA lesions (Figure 6, Supplementary Figure 6), mice were euthanized if they exhibited greater than 15% weight loss (representing the pre-defined humane endpoint). 6-OHDA lesion extent was evaluated via TH staining of the SNc at day 20 after injection of 6-OHDA, following testing in the chronic stage. Mice were excluded from analysis if the lesion exhibited less than 70% efficacy (the lesioned SNc exhibited greater than 30% of neurons relative to the intact side). For optogenetics, chemogenetics, and 6-OHDA lesions, exclusions were performed post-experimentally upon examination of the tissue.

Significance

A significant cross-correlation between angular velocity and ddF/F (Figure 1C) was defined as a peak within 0.5 s lag greater than (cross correlated) or less than (anti-cross correlated) 2 standard deviations of a normally distributed population mean:

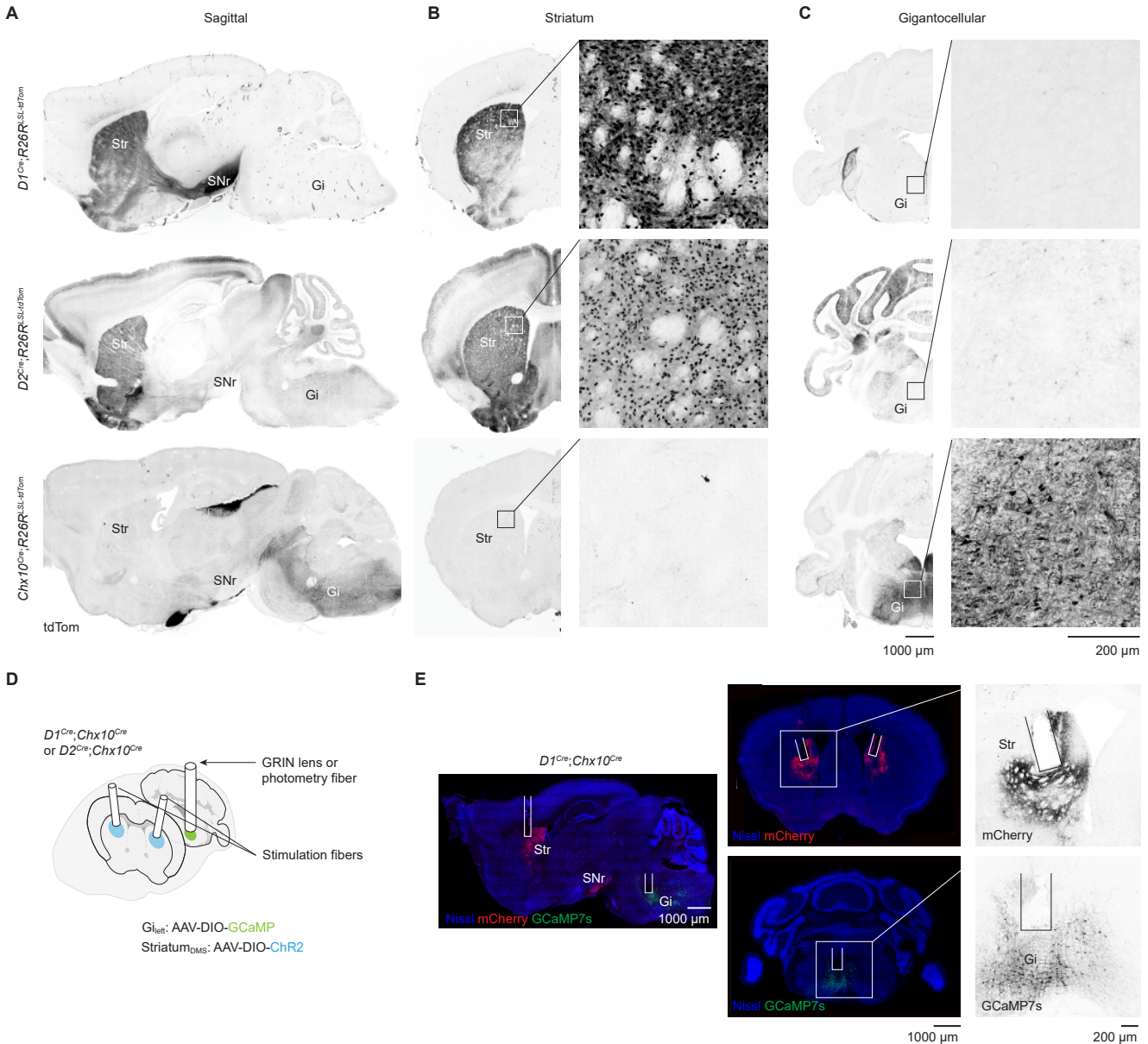
$$\mu \pm \frac{2}{\sqrt{n - |k|}}$$

where μ is the mean (zero), n is the number of observations, and k is the lag. For pairwise comparisons (Figures 2F, 3C,D, 4N, Supplementary Figure 2C), a two-tailed paired t-test was used to determine significance. For multiple comparisons, a one-way (Figures 1F, 2E, 4D,E,H,K, 5D, 6I, Supplementary Figures 2C, 3B,C, 4B,D, 5A-C, 6I) or two-way (Figures 6D,F, Supplementary Figures 6C,D,F) ANOVA—with repeated measures where appropriate—was used to determine whether significance was present. If significance was present, P values were assigned in multiple comparisons testing using Tukey's post-hoc test. Data was assumed to exhibit normal distribution, but this was not tested. $P < 0.05$ was considered statistically significant, with * $P < 0.05$, ** $P < 0.01$, and *** $P < 0.001$. P values and n values are reported in the figure legends. Full details on statistical analyses, including test statistics, and cohort composition are reported in Supplementary Table 1. Statistics were performed in GraphPad Prism 9.3.1.

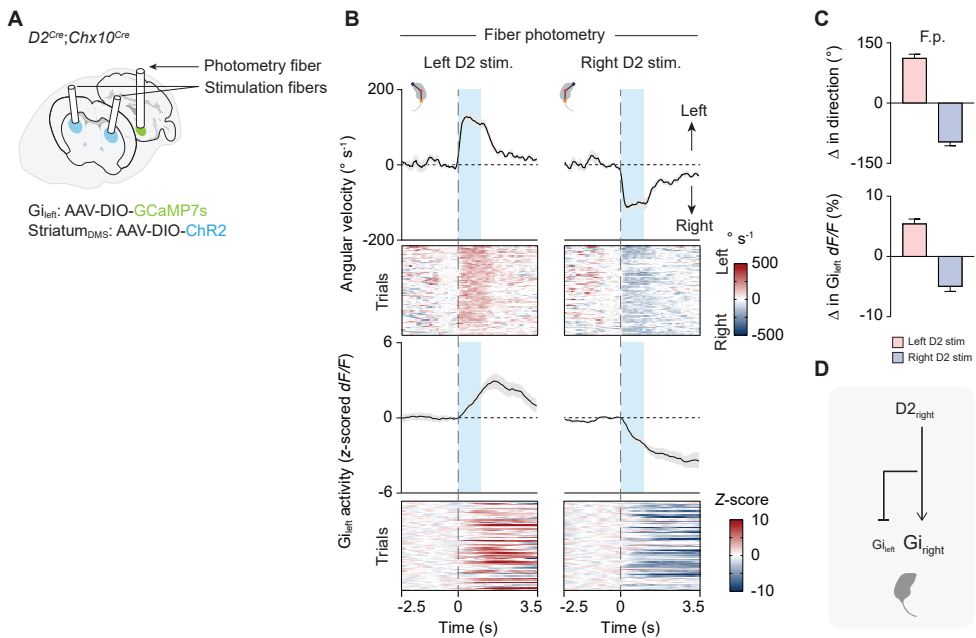
Plots

Time series graphs, heat maps, and box-and-whisker plots were generated in GraphPad Prism 9.3.1. Neuronal density plots in Figure 3E were generated using a custom script in RStudio. Time series data for angular velocity, direction, and dF/F z-score represent mean \pm standard error mean. Box-and-whisker plots represent the median, 25th and 75th percentiles, and range. Individual data points (n) are plotted for each comparison, where n values represent distinct mice—except for where indicated otherwise (Figures 1F, 2E, Supplementary Figures 2C, 3B,C). Figures were prepared in Adobe Illustrator, and videos were prepared in Adobe Premier Pro. Time series graphs in Supplementary Videos 1-8 were generated using custom MATLAB scripts.

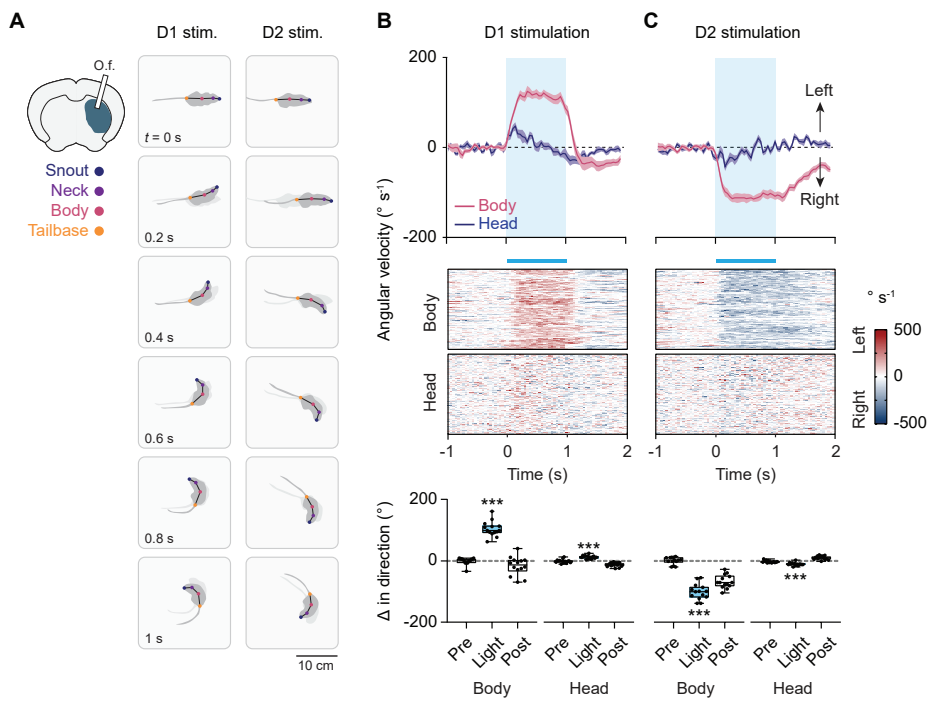
Supplementary Material



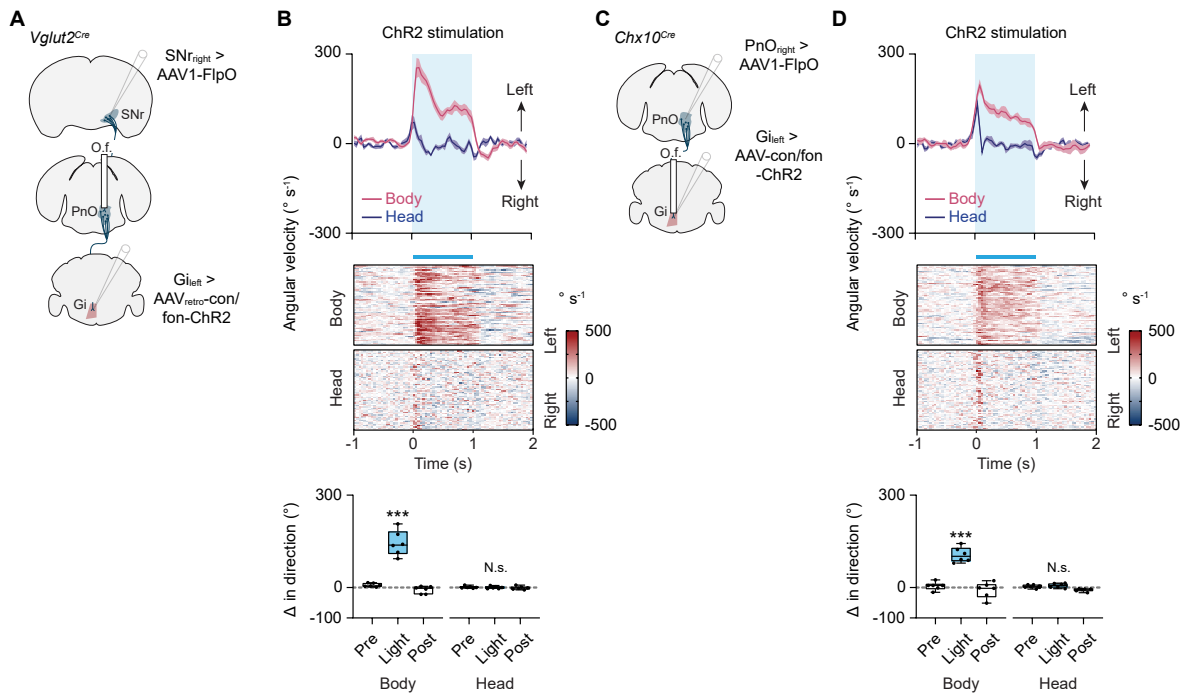
Supplementary Figure 1. Optogenetic stimulation of SPNs with simultaneous Ca^{2+} recording from *Chx10* Gi neurons. **A**, *D1^{Cre}* and *D2^{Cre}*, and *Chx10^{Cre}* alleles exhibit non-overlapping Cre expression within the striatum (Str) and nucleus gigantocellularis (Gi), respectively, in sagittal sections. *Top*, *D1^{Cre}* (Gensat EY217);*R26R^{LSL-tdTom}* mice exhibit tdTom expression in Str, with tdTom⁺ axons projecting to SNr. tdTom expression is largely absent from Gi. *Middle*, *D2^{Cre}* (Gensat ER44);*R26R^{LSL-tdTom}* mice exhibit tdTom expression in Str, whereas tdTom expression is largely absent from Gi. *Bottom*, *Chx10^{Cre};R26R^{LSL-tdTom}* mice exhibit tdTom expression in Gi, whereas tdTom expression is largely absent in Str. Sagittal images are representative of expression patterns observed in $n = 3$ mice for each genotype. **B**, In coronal sections including the striatum, *D1^{Cre};R26R^{LSL-tdTom}* and *D2^{Cre};R26R^{LSL-tdTom}* mice exhibit strong tdTom expression in Str, whereas *Chx10^{Cre};R26R^{LSL-tdTom}* mice exhibit scant tdTom expression in Str. **C**, In coronal sections including Gi, *D1^{Cre};R26R^{LSL-tdTom}* and *D2^{Cre};R26R^{LSL-tdTom}* mice exhibit scant tdTom expression in Gi. *D2^{Cre};R26R^{LSL-tdTom}* mice exhibit some tdTom expression in the neighboring IRT and PCrt. *Chx10^{Cre};R26R^{LSL-tdTom}* mice exhibit strong tdTom expression in Gi. Coronal images are representative of expression patterns observed in $n = 3$ -6 mice for each genotype. Scale bar (**A-C**) for overview sagittal and coronal images = 1.0 mm. Scale bar (**B, C**) for insets = 200 μm . **D**, Schematic of *Chx10* Gi_{left} GCaMP recording with optogenetic stimulation of left or right, D1 or D2 SPNs. **E**, Examples of bilateral ChR2-2A-mCherry expression and fiber implantation in the dorsomedial Str, and GCaMP7s expression and fiber implantation in Gi_{left} in *D1^{Cre};Chx10^{Cre}* dual-allelic mice. ChR2-2A-mCherry and GCaMP7s expression patterns are representative of $n = 7$ *D1^{Cre};Chx10^{Cre}* mice. *D2^{Cre};Chx10^{Cre}* mice exhibited similar ChR2-2A-mCherry and GCaMP7s expression patterns, with notable absence of mCherry⁺ axons in SNr ($n = 7$ mice).



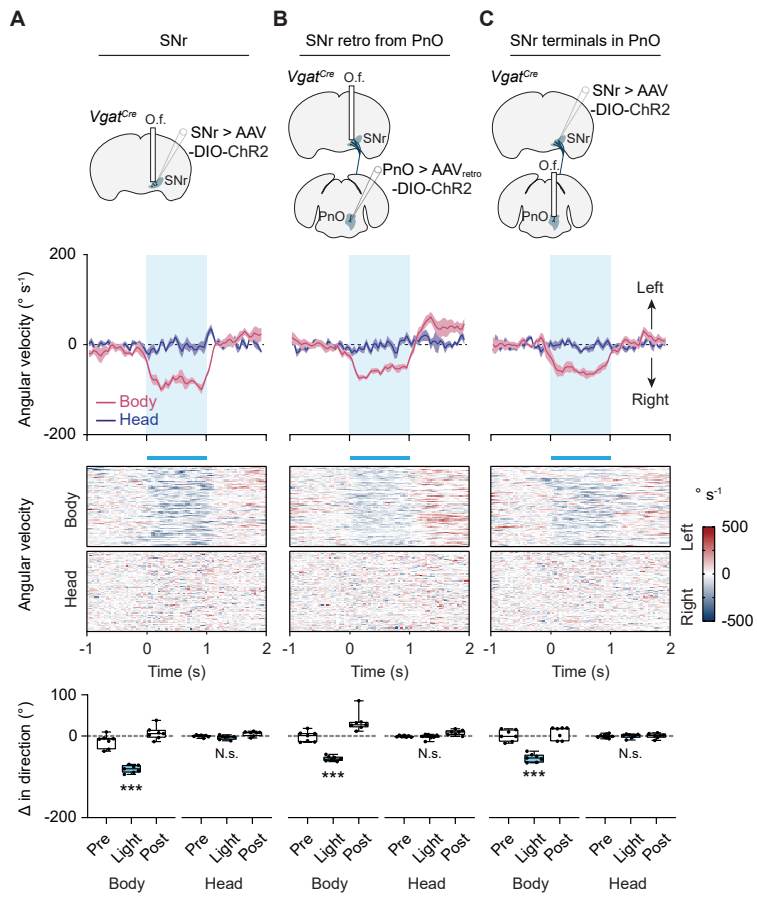
Supplementary Figure 2. Stereotypic modulation of *Chx10* Gi activity via unilateral activation of D2 SPNs. **A,** Schematic of *Chx10* Gi_{left} GCaMP7s recording with optogenetic stimulation of left or right D2 SPNs. **B,** Stimulation of D2 SPNs caused ipsiversive turns, with an increase in *Chx10* Gi activity ipsilateral to the stimulation and a decrease in *Chx10* Gi activity contralateral to the stimulation. $n = 7$ mice; 10 left and right D2 stimulation trials for each mouse. **C, Top**, Change in direction associated with 1 s ChR2 stimulation of left or right D2 SPNs. **Bottom**, Change in *Chx10* Gi_{left} dF/F activity associated with 1 s ChR2 stimulation of left or right D2 SPNs. The magnitude of the change in dF/F was similar for $D2_{right}$ versus $D2_{left}$ stimulation trials. $P = 0.81$; two-tailed paired t-test; $n = 7$ mice. See Supplementary Table 1 for full statistical analysis. **D,** Model for locomotor asymmetries caused by stimulation of D2 SPNs. Optogenetic stimulation of D2 SPNs has a contralateral inhibitory effect on *Chx10* Gi neurons, as well as an ipsilateral excitatory effect.



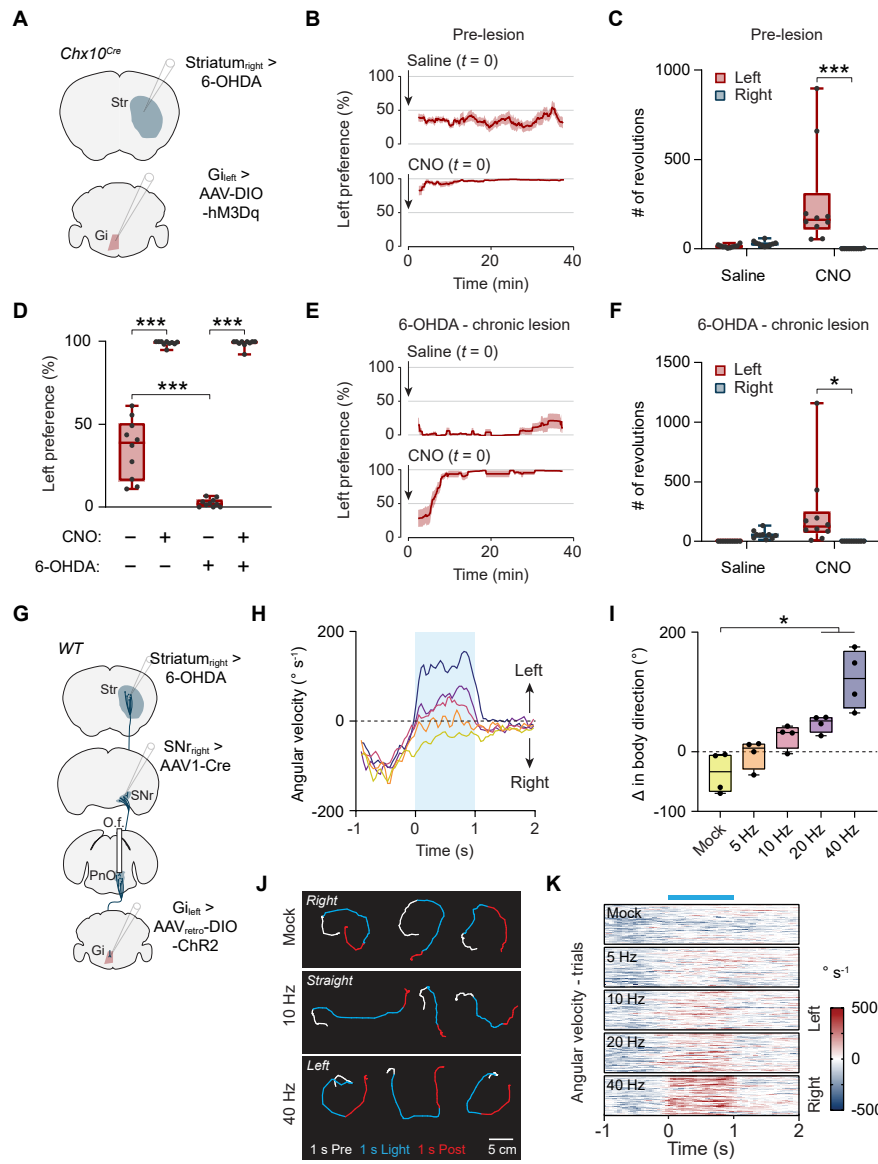
Supplementary Figure 3. Kinematic analysis for D1 and D2 SPN stimulation experiments. **A**, ChR2 stimulation of D1 or D2 SPNs caused rotation accompanied by contraction of the axial (head and trunk) musculature. For D1 SPNs ChR2-induced rotation was contraversive, whereas for D2 SPNs the rotation was ipsiversive. Contraction of axial musculature is interpreted as a change in the head angle relative to the upper body (contraction of the splenius capitis), or as a change in the angle of the upper body relative to the lower body (contraction of trunk musculature, including the abdominal obliques). Representative example from $n = 14$ fibers implanted in 7 mice. **B**, Stimulation of D1 SPNs causes changes in both body and head orientation. Body, $***P = 7.7 \times 10^{-10}$; head, $***P = 4.5 \times 10^{-4}$; one-way ANOVA with Tukey's multiple comparison test; $n = 14$ fibers implanted in 7 mice (where n is the average of 10 trials for each fiber). **C**, Stimulation of D2 SPNs causes changes in both body and head orientation. Body, $***P = 5.3 \times 10^{-9}$; head, $***P = 6.4 \times 10^{-4}$; one-way ANOVA with Tukey's multiple comparison test; $n = 14$ fibers implanted in 7 mice (where n is the average of 10 trials for each fiber). Data in A-C represent extended analysis of the data presented in Figure 2C, Supplementary Figure 2B.



Supplementary Figure 4. Projection and cell type-specific ChR2 interrogation of the PnO → Gi pathway. **A,** Strategy for stimulating Vglut2⁺ neurons in PnO which receive input from SNr_{ipsi} and project to Gi_{contra}. In *Vglut2^{Cre}* mice, AAV_{retro-con}/fon-ChR2 was injected in Gi_{left} followed by AAV1-FlpO in SNr_{right}. An optic fiber (O.f.) was then implanted over PnO. **B,** Optogenetic stimulation of PnO-Vglut2_{contra} neurons using the strategy in (A) evoked contraversive turning. Body, ***P = 5.6 x 10⁻⁴; head, P = 0.90; one-way ANOVA with Tukey's multiple comparison test; n = 6 mice (where n is the average of 10 trials for each mouse). **C,** Strategy for stimulating Chx10⁺ neurons in Gi which receive input from the PnO_{contra}. In *Chx10^{Cre}* mice, AAV1-FlpO was injected in PnO_{right} followed by AAV-con/fon-ChR2 in Gi_{left}. An optic fiber was then implanted over Gi. **D,** Optogenetic stimulation of PnO recipient, Chx10⁺ Gi neurons evoked ipsiversive turning. Body, ***P = 1.3 x 10⁻⁴; head, P = 0.80; one-way ANOVA with Tukey's multiple comparison test; n = 6 mice (where n is the average of 10 trials for each mouse).



Supplementary Figure 5. ChR2 interrogation of the Vgat⁺ SNr → PnO projection. **A,** ChR2 stimulation of Vgat⁺ SNr neurons caused ipsiversive turning. Body, *** $P = 1.8 \times 10^{-4}$; head, $P = 0.43$; one-way ANOVA with Tukey's multiple comparison test; $n = 7$ mice (where n is the average of 10 trials for each mouse). **B,** The ipsiversive turning phenotype using the strategy in (A) was partly recapitulated by stimulating Vgat⁺ neurons in SNr that were retrogradely targeted from PnO. Body, *** $P = 5.4 \times 10^{-5}$; head, $P = 0.95$; one-way ANOVA with Tukey's multiple comparison test; $n = 7$ mice (where n is the average of 10 trials for each mouse). **C,** The ipsiversive turning phenotype using the strategy in (A) was partly recapitulated by stimulating Vgat⁺ SNr terminals in PnO. Body, *** $P = 8.3 \times 10^{-5}$, head, $P = 0.98$; one-way ANOVA with Tukey's multiple comparison test; $n = 7$ mice (where n is the average of 10 trials for each mouse).



Supplementary Figure 6. Restoration of contraversive turning gaits in mice with chronic unilateral striatal dopamine depletion. **A**, Strategy for restoring contraversive turning in mice with unilateral striatal dopamine depletion. *Chx10* Gi_{left} neurons were targeted for expression of excitatory hM3Dq-DREADDs (Gi_{left} > DIO-hM3Dq in *Chx10^{Cre}* mice). Mice underwent testing prior to a unilateral 6-OHDA lesion targeting SNc → DMS projection neurons (Striatum_{right} > 6-OHDA), and were tested again after 6-OHDA lesion in both the acute (4–6 days) and chronic (15–19 days) stage. **B–C**, Pre-lesion testing of *Chx10^{Cre}* mice with Cre-dependent expression of hM3Dq-DREADDs in Gi_{left}. **B**, Analysis of left vs. right movement preference in the open field, quantified as the percentage of left revolutions relative to the total number of revolutions 10–40 minutes after injection of saline or CNO at *t* = 0. CNO administration caused a predominantly leftward movement preference in a time-dependent manner. **C**, Number of left and right revolutions quantified between 10–40 min after injection of saline or CNO. CNO left vs. CNO right, ****P* = 9.0 × 10⁻⁴; two-way ANOVA with Tukey's multiple comparison test; *n* = 10 mice. **D**, Mice with chronic unilateral striatal dopamine depletion exhibited a loss of contraversive (left) turning gaits (−CNO/+6-OHDA). CNO administration (+CNO/+6-OHDA) reversed ipsiversive (right) rotational biases and restored contraversive (left) turning gaits. −CNO/−6-OHDA vs. +CNO/−6-OHDA, ****P* < 1.0 × 10⁻¹⁵; −CNO/−6-OHDA vs. −CNO/+6-OHDA, ****P* = 8.6 × 10⁻⁹; −CNO/+6-OHDA vs. +CNO/+6-OHDA, ****P* < 1.0 × 10⁻¹⁵; two-way ANOVA with Tukey's multiple comparison test; *n* = 10 mice. Pre-lesion data (−6-OHDA) is also presented in Figure 6D. **E**, Mice with chronic unilateral striatal dopamine depletion exhibited predominantly ipsiversive (right) movement preference. CNO administration at *t* = 0 reversed ipsiversive rotational biases in a time-dependent manner, restoring contraversive turning gaits within 10 minutes. **F**, Number of left and right revolutions quantified in mice with chronic unilateral striatal dopamine depletion 10–40 min after injection of saline or CNO. CNO left vs. CNO right, ****P* = 0.017; two-way ANOVA with Tukey's multiple comparison test; *n* = 10 mice. **G**, Strategy for testing the efficacy PnO-Vglut2_{contra} neurons in restoring contraversive turning in mice with chronic unilateral striatal

dopamine depletion. **H**, Average body angular velocity associated with mock stimulation (no light) or 1 s ChR2 stimulation at different frequencies. Optogenetic stimulation of PnO-Vglut2_{contra} neurons reversed ipsiversive rotational biases associated with chronic unilateral striatal dopamine depletion, restoring straight locomotion at low frequencies (5 Hz, 10 Hz) and contraversive turning gaits at high frequencies (20 Hz, 40 Hz). **I**, Quantification of the change in body direction during 1 s mock stimulation or ChR2 stimulation at different frequencies. Mock vs. 20 Hz, * P = 0.021; Mock vs. 40 Hz, * P = 0.029; one-way repeated measures ANOVA with Tukey's multiple comparison test; n = 4 mice (where n is the average of 10 trials for each mouse). **J**, Example trajectories associated with mock stimulation (no light) or 1 s ChR2 stimulation at 10 Hz or 40 Hz. 10 Hz stimulation restored straight walking during stimulation, while 40 Hz stimulation restored contralateral turning gaits. **K**, Trial-by-trial analysis of angular velocity during mock stimulation or ChR2 stimulation at different frequencies. Each plot contains 40 individual trials from n = 4 mice (10 trials per mouse).

Supplementary Table 1. Statistics summary. The table reports statistical methods employed, test statistics, and cohort composition for each data set.

Supplementary Video 1. Endoscopic Ca^{2+} imaging of *Chx10* Gi neurons. Related to Figure 1.

Supplementary Video 2. Examples of spontaneous left turns, straight events, and right turns segmented from angular velocity time series. Related to Figure 1.

Supplementary Video 3. Examples of turns evoked via D1- or D2-SPN stimulation. Related to Figure 2 and Supplementary Figures 2, 3.

Supplementary Video 4. Optogenetic stimulation or inhibition of PnO-Vglut2_{contra} neurons. Related to Figure 4.

Supplementary Video 5. Tight control of turning kinematics via frequency-dependent modulation of PnO-Vglut2_{contra} neurons. Related to Figure 4.

Supplementary Video 6. Optogenetic inhibition of Vgat⁺ SNr neurons. Related to Figure 5.

Supplementary Video 7. Chemogenetic activation of *Chx10* Gi neurons in mice with acute unilateral striatal dopamine depletion. Related to Figure 6. Representative examples are taken from early (0-10 min), intermediate (10-20 min), or late stages (> 20 min) following administration of CNO.

Supplementary Video 8. Optogenetic activation of PnO-Vglut2_{contra} neurons in mice with acute unilateral striatal dopamine depletion. Related to Figure 6.